International Journal of Rock Mechanics and Mining Sciences 118 (2019) 1–20

Contents lists available at ScienceDirect

International Journal of Rock Mechanics and Mining Sciences

journal homepage: www.elsevier.com/locate/ijrmms

Stress magnitudes in the Basel enhanced geothermal system

Benoît Valley[a,*], Keith F. Evans[b]

[a] Center for Hydrogeology and Geothermics, University of Neuchâtel, Switzerland
[b] Institute of Geophysics, ETH Zürich, Switzerland

ABSTRACT

This paper presents the results of an evaluation of stress magnitudes in the granitic EGS reservoir in Basel, Switzerland. The profile of minimum principal horizontal stress, *Shmin*, is constrained by hydraulic tests, but the magnitude of the maximum horizontal principal stress, *SHmax* is uncertain. Here we derive estimates for *SHmax* by analysing breakout width data from an acoustic televiewer logs run in the granitic basement section of the BS-1 borehole. Some 81% of the borehole in the granite is affected by breakouts. The approach employed to derive *SHmax* magnitude from the estimated breakout widths is taking into account all stress components at the borehole wall including the remnant thermal stress arising from the cooling of the borehole wall by the drilling. In BS-1, breakouts width tends to decrease with depth. Assuming there is no significant systematic change in the strength characteristics of the rock along the length of the hole, for which there is no evidence, the large-scale trend has the consequence of implying a small gradient of the *SHmax* profile. A low *Shmin* gradient was also implied by a stress analysis that additionally considered the occasionally coincident presence of drilling induced tension fractures. The absolute values of *SHmax* depend upon the failure criterion used. Criteria that consider the strengthening effect of the intermediate stress (Mogi-Coulomb and Hoek-Brown 3D) yield profiles that violate frictional limits on the strength of the crust above 4 km, whereas the profiles of the Mohr-Coulomb and Rankine criteria do not. The Mohr-Coulomb criteria profiles indicate a trend in *SHmax* from favoring strike-slip faulting above 4200 m to strike-slip/normal faulting below. This is consistent with focal mechanisms recorded during the reservoir stimulation which show a mix of strike-slip and normal faulting throughout the depth range considered.

1. Introduction

The hydraulic stimulation of low-permeability Enhanced/Engineered Geothermal System (EGS) reservoirs is necessary for such systems to produce commercially interesting flow rates. The in-situ state of stress plays a major role in the response of the rock mass to hydraulic stimulation injections. Thus, it is a key parameter that must be specified in any geomechanical model of the stimulation process. It is, however, not straightforward to quantify the state of stress because direct methods that measure the complete stress tensor are difficult to apply in deep boreholes. The estimation of the stress state is best approached by drawing upon constraints arising from a variety of sources including hydraulic injection records, geophysical logging data, interpretation of passive seismic records, rock testing data and observation of borehole wall failure.

The theoretical background and the overall approach to characterizing the stress state in deep boreholes is well documented in the literature.[1–3] However, the approach taken at a given site will depend upon the available datasets and the site-specific conditions. Within the context of deep crystalline rocks, there are several examples where wellbore failure has been used to constrain stress magnitudes. Both breakouts and drilling-induced tension fractures (DITFs) were used to constrain stress magnitudes in the KTB research hole[4–7] in Germany. Breakouts occurring in the Cajon Pass research borehole in California, were used to estimate the in-situ stress magnitudes[8] and the presence of faults was shown to locally alter the stress orientation and magnitudes.[9] The thermal conditions at wellbore wall were particularly important for stress analyses from wellbore failure performed at the geothermal project of Soultz-sous-Forêts.[10–13] This was also the case at the Habanero geothermal project in Australia where breakouts and DITFs were used to obtain point estimates of horizontal stress magnitudes. It was also shown that strong cooling enhances borehole stability.[14] In all these studies, a major limitation came from the difficulty to obtain a reliable strength estimate for the borehole walls. In the 5 km deep Basel-1 well, borehole breakouts occur over 81% of the lowermost 2.6 km in granite, together with occasional DITFs. Thus, the wellbore failure observations provide a rich source of stress information for this site. In this paper, we present an analysis of the wellbore failure observed in the 5 km deep well, and supplement this with other information from the site to obtain profiles of stress magnitudes to 5 km for the Basel EGS reservoir.

A complete characterization of the stress field would require the estimation of six independent stress parameters (tensor quantity) at every point in the reservoir. However, it is common practice to reduce the number of unknowns by making some reasonable assumptions about the prevailing stress state. The first concerns gravity, which has a

* Corresponding author.
E-mail address: benoit.valley@unine.ch (B. Valley).

https://doi.org/10.1016/j.ijrmms.2019.03.008
Received 22 July 2018; Received in revised form 24 November 2018; Accepted 9 March 2019
Available online 06 April 2019
1365-1609/

first order effect on the stress state. Since the topography at the Basel site is relatively flat compared to the depth of our analyses, we make the assumption that one principal stress is vertical and has a magnitude, *Sv*, equal to the overburden. As the latter can be estimated from density logs, this reduces the stress characterization to determining the magnitude of the maximum and minimum principal horizontal stresses, *SHmax* and *Shmin* respectively, and the orientation of either *SHmax* or *Shmin*. We also assume that the magnitudes of *Sv*, *SHmax* and *Shmin* follow linear trends with depth (at least within relatively homogenous domains). We recognize that heterogeneities and discontinuities in the rock mass induce variations in the stress field, i.e. that the stress components will locally depart from the characterization that is made within the assumptions stated above. The study of the heterogeneities in the stress field is a topic of importance that is not investigated in any detail in this study. The objective here is to derive a robust first order characterization of the stress field in the Basel EGS reservoir that can be used to provide input for geomechanical simulation of the reservoir. We begin by describing the current state of knowledge on the stress state in the crystalline basement underlying the Basel EGS site. We then use data sets from the deep geothermal borehole BS-1 of the project to further constrain the stress characterization at the site.

2. Previous studies on the state of stress at the Basel enhanced geothermal system

In 2006, a 5 km deep borehole was drilled below the city of Basel (Switzerland) with the intention of developing an Enhanced/Engineered Geothermal System (EGS) within a granite body whose weathered top lies beneath 2426 m of sedimentary cover.[15] After an extensive reservoir characterization phase, the entire open hole section between 4632 m and 5009 m was subject to a hydraulic stimulation injection in December 2006 as the first stage in creating a heat exchanger within the granite. This stimulation injection produced seismicity that was felt in the city of Basel, which eventually resulted in the abandonment of the project.

The average orientation of the maximum horizontal principal stress in the basement of the southern part of the Upper Rhine Graben and the Swiss foreland region centred on Basel is well defined from failure analyses in deep boreholes[16,17] and stress inversion of focal mechanisms.[18] The results are consistent with the observation of borehole failure in the 5 km deep BS1 borehole that indicate a mean *SHmax* orientation of 143° ± 14°.[17]

Focal mechanisms of natural seismicity in the area show a mix of strike-slip and normal faulting, with strike-slip being dominant in the southern end of the Upper Rhine Graben.[18–20] Analyses of microseismicity induced by the hydraulic stimulation of the BS-1 hole also predominantly indicate a mix of strike-slip and normal faulting regimes.[20–23]

Häring et al.[15] proposed an initial characterization of the stress magnitude in the Basel EGS reservoir that is consistent with a strike slip regime. Their characterization is based on various indicators, including a single RACOS (Rock Anisotropy Characterization on Samples[24]) measurement on a core sample recovered from 4911 m. The principle of the RACOS measurement is similar to residual strain analyses,[25] but in the case of the RACOS approach, P- and S- wave velocities are measured and used in the analyses. The details of the analysis, however, are not disclosed, and thus the robustness of the estimate cannot be assessed. Hence, the RACOS results are not included in our analysis.

A profile for vertical stress in the open-hole section below 4623 m was derived by Häring et al.[15] The density profile of the sedimentary section, which is constituted of sandstones from the Permian, evaporates, shales and carbonates from the Trias, carbonate and marl from the Jurassic and mostly marls from the Cenozoic,[15,17] was estimated from density logs run over sections of the 1 km distant well Otterbach-2, supplemented by average formation densities given by Schärli and Kohl.[26] Combining this with the density log from the granitic section of BS-1, they estimated a mean density for the rock overlying the open hole section of $\rho = 2538\ \mathrm{kg/m^3}$, giving an *Sv* profile of:

$$Sv\,[MPa] = \rho g z = 24.9 z\,[km] \quad (1)$$

where g is the gravitational acceleration ($= 9.81\ \mathrm{m/s^2}$) and z is the depth below ground surface (BG) in km. In this paper compression is taken as positive. The mean density of the granite section below 2426 m BG is $2683\ \mathrm{kg/m^3}$, somewhat higher than the mean value above, giving a steeper gradient of 26.3 MPa/km for the granitic section. Taking into account the density data for the sedimentary section used by Häring et al.[15] gives a *Sv* profile for the granitic section of: $Sv\,[MPa] = 26.3 z\,[km] - 4.0$. The estimate of Eq. (1) is a convenient simplification for our analysis. It is exact at 2857 m depth, but overestimates *Sv* by 0.6 MPa at the top of the granite, and underestimates *Sv* by 3.0 MPa at the hole bottom (5004 m).

The *Shmin* estimate from Häring et al.[15] is constrained by a RACOS measurement at 4902 m of 84 MPa and the maximum injection pressure reached during hydraulic stimulation of 74 MPa at the casing shoe at 4632 m. A best linear fit forced through 0 MPa on surface gives a *Shmin* profile of $Shmin\,[MPa] = 17.1 z\,[km]$. The RACOS measurement for *SHmax* at 4902 m depth indicates a magnitude of 160 MPa. A linear fit forced through this datapoint and 0 MPa on surface produces a *SHmax* profile of $SHmax\,[MPa] = 32.6 z\,[km]$, which is close to a frictional limit derived assuming the strength of the rock mass is limited by cohesionless and optimally oriented planes of weakness with a friction coefficient $\mu = 0.6$.[15] Häring et al.[15] warn that the RACOS measurement should be treated with caution, and propose instead a broad range of *SHmax* estimates with upper and lower values derived from the friction limit approach with friction coefficients of 1.0 and 0.6 respectively. Evidently, significant uncertainties remain regarding the horizontal stress magnitude profiles along the BS-1 well.

3. Constraints from hydraulic injection tests

The profile of *Shmin* is best estimated from hydrofracture tests. In deep wells in the oil and gas sector, conventional hydrofracture or 'minifrac' tests are rarely conducted owing to operational difficulties and risks in hydraulically isolating short open-hole test intervals. Rather, *Shmin* estimates are usually extracted from FITs (Formation Integrity Tests), LOTs (Leak-off tests), or XLOTs (Extended Leak-off Tests).[27] The nomenclature is sometimes ambiguous concerning the exact configuration of such tests.[28] We are referring here to small-volume injection tests performed on a short (~10 m) section of hole drilled ahead of a casing shoe after cementing a casing to test the integrity of the cement seal and determine the pressure at which the injectivity of the formation begins to increase due to the opening of fractures. It is usually not known whether a natural or an induced fracture opens - and thus whether the opening pressure is a direct measure of the minimum principal horizontal stress or is greater. Only XLOT tests feature pressurization cycles, which are necessary to demonstrate that the increase in permeability is reversible, and most likely due to mode-1 fracture opening, as required for the pressure to be representative of the normal stress on the fracture that opens. FITs and LOTs are ambiguous in this regard, and may show permeability increases due to shearing at pressures much lower than the level of the minimum principal stress. FITs, unlike XLOTs, may yield underestimates for *Shmin*, but both can yield overestimates. A FIT test was performed in the granitic basement at 2602 m BG immediately after cementing the 10.75″ liner by injecting water at 10 l/min and monitoring the pressure build-up (Fig. 1). A deviation towards flattening from the linearly-increasing pressure curve was observed at a downhole pressure of 34 MPa, although it is not entirely clear whether pressure would have continued to increase had injection not been terminated. If 34 MPa is taken as a direct measure of *Shmin* at 2602 m BG, and the *Shmin* profile is assumed to be linear and passes through the origin (i.e. *Shmin* is zero at the surface), then the value of *Shmin* at the top of the

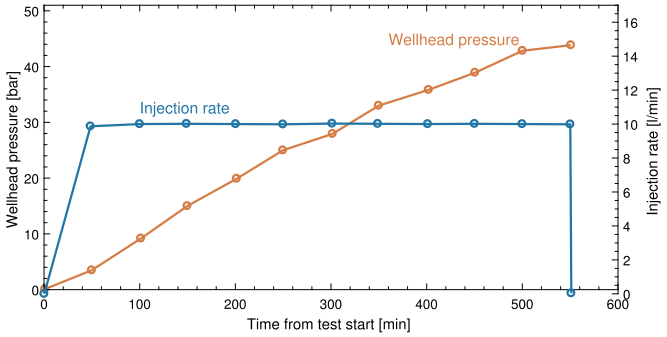

Fig. 1. Pressure and flow rate record during the FIT test at a depth of 2602 m BG on August 9th, 2006. The maximum wellhead pressure reached is 43 bars. At the time of test, the borehole fluid had a density of 1160 kg/m3 which implies a downhole pressure of 34 MPa at the depth of the test.

open hole section at 4632 m would be 60.6 MPa. The *Shmin* profile would be similar to that found at the Soultz EGS site inasmuch as *Shmin* would be about 52% of the vertical stress.[13] However, since the wellbore pressure at 4632 m reached 74.4 MPa towards the end of the stimulation injection, the extrapolated *Shmin* profile from the FIT measurement would imply that the borehole pressure exceeded *Shmin* at the casing shoe by 13.8 MPa. Such a large excess is implausible, particularly as there are well-developed drilling-induced tension fractures at the top of the open hole that would surely extend as hydrofractures under such a high overpressure. For this reason, the best estimate of *Shmin* at 4632 m (the 7–5/8″ liner shoe) is taken as 74.4 MPa, the maximum pressure reached during the stimulation injection. Evidence at Soultz suggests that the maximum pressure attained at the top of the open hole section represents a reasonable measure of *Shmin* at that depth, although this is probably not a universal rule.[13] Assuming a linear *Shmin* trend that passes through the origin, this *Shmin* measure at 4632 m leads to the following linear trend:

$$Shmin\,[MPa] = 16.06z\,[km] \tag{2}$$

where z is in kilometres. This is slightly less than the value of 17.1 z [km] MPa adopted by Häring et al.,[15] which is influenced by a single RACOS measurement on core taken from near 4900 m.[24] Considering a linear fit through both the FIT test result at 2602 m and the maximum pressure reached at the liner shoe (4632 m) leads an even larger gradient with a large negative offset at zero depth:

$$Shmin\,[MPa] = 19.90z\,[km] - 17.78 \tag{3}$$

In the following analyses, the pore pressure will be considered to be given by hydrostatic conditions with a fluid density of 1000 kg/m^3:

$$Pp\,[MPa] = \rho_f g z = 9.81z\,[km] \tag{4}$$

This a reasonable assumption, although a slight reservoir overpressure of 1.7–2.6 MPa is reported by Häring et al.[15] shortly after drilling.

The basement section of the well was drilled with a potassium-silicate mud whose density varied from 1060 to 1160 kg/m^3 over the drilling operations. The density during the acquisition of the acoustic televiewer data used in our study was 1080 kg/cm^3 which implies that the entire basement has been exposed to this mud density. For simplicity we used in our analysis a mud pressure profile equal to our pore pressure profile ($Pw = Pp$). This has a minor impact on our stress analyses of less than 2 MPa at 2.5 km and less than 4 MPa at 5 km depth.

The *SHmax* profile is the most difficult to constrain and is the focus of this paper. Specifically, we will derive *SHmax* estimates from the width of borehole breakouts and then add constraints from the occasional presence of both breakouts and drilling-induced tension fractures (DITFs). These analyses begin by considering the stress concentrations arising at the borehole wall.

4. Constraints from wellbore failure

One approach to stress characterization that is now commonly applied is to estimate *SHmax* from the width of breakouts.[29] However, this approach relies heavily on the appropriateness of the failure criteria used in the analyses[8] since different failure criteria can lead to significantly different *SHmax* estimates. For example, criteria that include the strengthening effect of the intermediate principal stress give significantly higher *SHmax* magnitude estimates compared to those that consider only the minimum and maximum principal stress. Irrespective of the failure criterion used, it is often difficult to parametrize the criterion chosen so that it represents the in-situ strength characteristics of the rock in question. Such parameter values are usually estimated from mechanical tests on a few core samples. The paucity of data limits our ability to quantify strength variability, and hinders the assessment of the representativeness of the parameter estimates to in-situ conditions. In addition, core damage due to the relaxation of in-situ stresses and attendant formation of micro-cracks when coring is likely to lead to an underestimation of the in-situ strength.[30] An alternative approach is to estimate in-situ strength using physical properties obtained from borehole logs.[31] However, the correlations underlying this approach will not yield robust constraints on rock strength. Despite these potential limitations, analyses of borehole failure provide some constraints on *SHmax* magnitude, particularly when the intensity or style of borehole failure varies with depth.[13] Matching these depth dependent variations, for example, a transition with depth from drilling induced tension fractures (DITFs) to breakouts as observed in the deep boreholes of Soultz-sous-Forêts,[13] imposes useful bounds on admissible *SHmax* magnitudes.

4.1. Borehole failure in the BS-1 borehole

Borehole failure in the BS-1 hole was identified on a Schlumberger ultrasonic borehole televiewer (UBI) log run in crystalline rock between 2569 and 4992 m shortly after drilling was completed.[17] The borehole diameter is 9-7/8” (25.1 cm) from 2594 to 4841 m depth (all depths in this paper are measured along hole from ground level) and 8–1/2” (21.6 cm) below. The borehole is sub-vertical, the maximum deviation reaching 8° towards the NW at 4600 m. The ultrasonic reflectivity and travel time logs are shown in Fig. 2a and b. Breakouts were identified along 81% of the logged section, and are almost continuous except for a large 152 m gap from 2747 to 2899 m depth, and some other less-significant gaps at 3820–3856 m, 4185–4221 m and 4582–4631 m.[17]

The procedure to determine borehole failure is described in Valley and Evans[17] and is summarized here. Only axial spalling occurring in two localized, diametrically-opposite directions were considered as potential breakouts. The breakouts were measured on successive 40 cm sections over which the borehole geometry was averaged. The angular width of both limbs of the breakouts were measured independently.

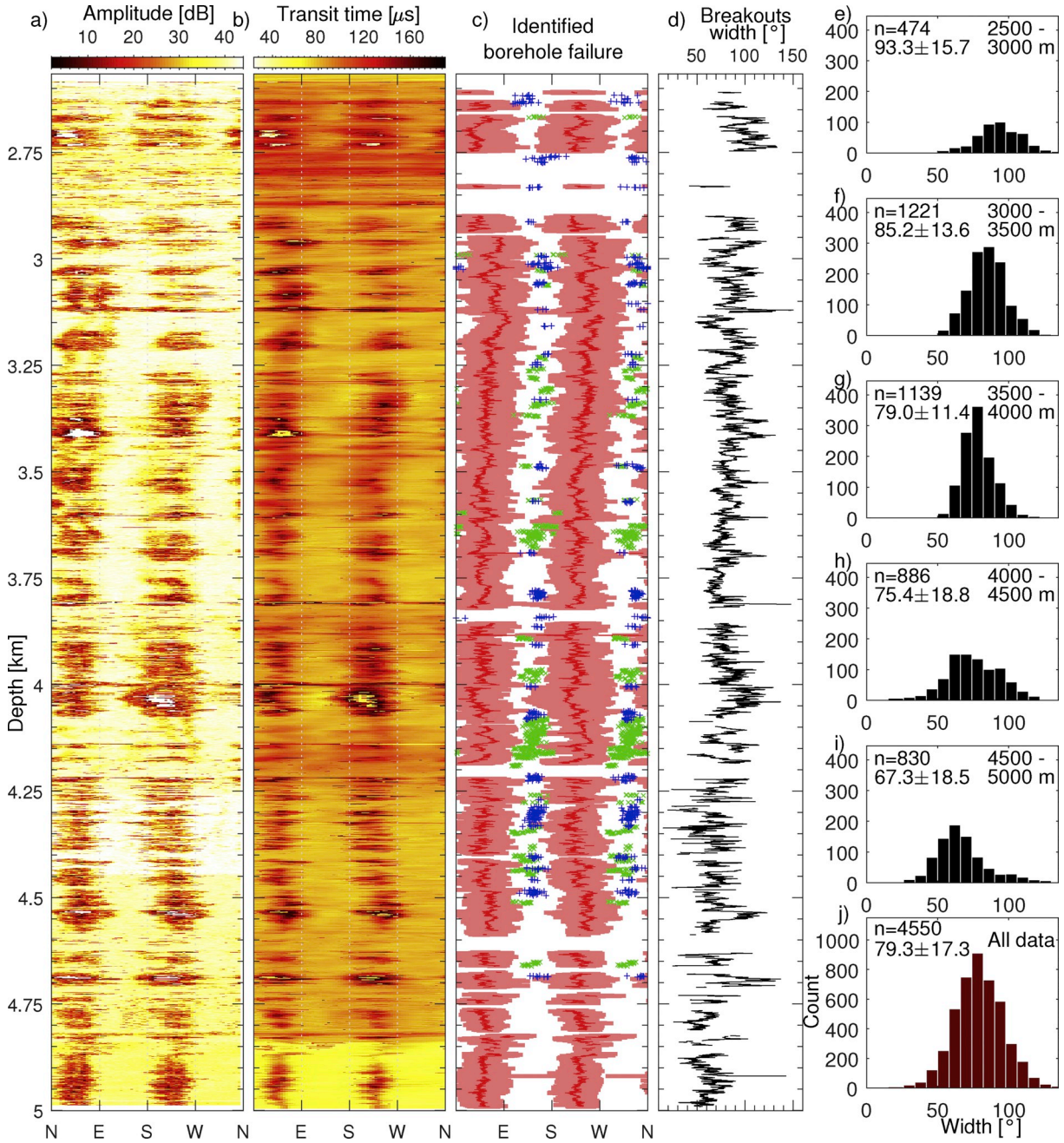

Fig. 2. a) Ultrasonic reflectivity. b) Ultrasonic travel time. c) Sketch of identified stress induced borehole failure. Red lines: breakout centres. Light red area: breakout span. Blue crosses: A-DITFs. Green crosses: E-DITFs strike. D) Breakout width profile from averaging the width of both limbs. e) to i) Histograms of breakout width for successive 500 m depth intervals and j) Histograms for all breakouts width data.

Measurements were made through visual inspection of borehole cross-sectional geometry. The identified breakouts are shown in red on Fig. 2c. The widths of each pair of breakout limbs are reasonably consistent except for a discrepancy near 4050 m m depth where the SW breakout side is more developed. For further analysis, the widths of both breakout limbs were averaged to generate the depth profile of breakout width shown in Fig. 2d. Histograms of breakout width for successive 500 m depth slices are presented on Fig. 2e–j. Considering all measurements, the width is 79.2° ± 17.4° (mean ± 1 std. Dev.). The smallest measured width is 20° with a single measurement exception at 15°. This is consistent with the theoretical consideration discussed in Section 4.4 which suggests that breakouts with width smaller than about 20° are not stable. The largest measured width is 150°. Breakout width tends to decrease with depth from an average of 93.3° in the 2500–3000 m range to 67.3° in the 4500–5000 m range.

For the DITFs, we distinguished between axial drilling-induced tension fractures (A-DITFs[32]) and en-echelon drilling induced tension fractures (E-DITFs[5]). Image features can be mistakenly identified as A-DITFs on borehole logs affected by stick-slip motion of the logging sonde.[33] Stick-slip occurred below 4701 m in the BS1 data set. E-DITFs and natural fractures can also be difficult to differentiate and some subjectivity is inherent to the image interpretations. Similar to borehole breakouts, the orientation of each limb of each A-DITFs with respect to the borehole center was measured every 40 cm independently. The orientation of each E-DITF pair was measured by fitting a sinusoid through the pair of limbs and determining the strike. The strikes of the A-DITFs and E-DITFs are presented on Fig. 2 as blue and green crosses respectively. Drilling-induced tension fractures are more sporadic than

borehole breakouts. In all, 245 m (10%) of the logged section in BS1 was affected by ADITFs and E-DITFs are observed along 314 m of borehole (13%). Altogether, drilling induced tensile failure affect slightly less than a quarter (23%) of the analysed borehole length.

In order to extract stress information from the wellbore failure observations, we need to consider the stress distributions prevailing at the borehole wall during the formation of the features. We begin by reviewing relevant theoretical considerations concerning the stress at the borehole wall and the failure criteria that feature in this study.

4.2. Stress state at the borehole wall

We will assume that borehole failure initiates at the borehole wall, and thus only the stress state at the wall is relevant for determining the breakout width and the formation of DITFs. The borehole BS-1 is taken as vertical since the deviation from verticality between 2600 and 4500 m ranges between 1 and 5°, and is close to 8° below 4500 m. We also assume that one principal stress is vertical and thus co-axial with the borehole axis. An extension of the analysis to the more general case where the borehole is not aligned with a principal stress axis could be made using the approach of Hiramatsu and Oka,[34] but is not required here as the effect of the limited borehole deviation on the estimated stress magnitude is considered to be minor.

The total stress state at the circular borehole wall can be expressed in cylindrical coordinates (see Fig. 3 for variables definitions) by the principal stress components of the tangential stress, S_θ, the radial stress, S_r, and the axial stress, S_z. Assuming far-field stress magnitudes, *Sv*, *SHmax* and *Shmin*, and a wellbore fluid pressure of *Pw*, the magnitudes of the components at an angle θ from the *SHmax* direction are[35]:

$$S_r = Pw + S_r^{\Delta T} \tag{5}$$

$$S_\theta = Shmin + SHmax - 2(SHmax - Shmin)cos(2\theta) - Pw + S_\theta^{\Delta T} \tag{6}$$

$$S_z = Sv - 2\nu(SHmax - Shmin)cos(2\theta) + S_z^{\Delta T} \tag{7}$$

where ν is Poisson's ratio, and $S_r^{\Delta T}$, $S_\theta^{\Delta T}$ and $S_z^{\Delta T}$ are possible thermal stress components in the radial, tangential and axial directions arising from any difference in rock temperature, ΔT, at the borehole wall from ambient temperature. Here, compression is taken positive. The thermal stress components at the borehole wall are given by Stephens and Voight[36] as:

$$S_r^{\Delta T} = 0 \tag{8}$$

$$S_\theta^{\Delta T} = S_z^{\Delta T} = \frac{\alpha E \Delta T}{1 - \nu} \tag{9}$$

where E is the Young's modulus, α in the coefficient of linear expansion, and ΔT is positive for heating and negative for cooling.

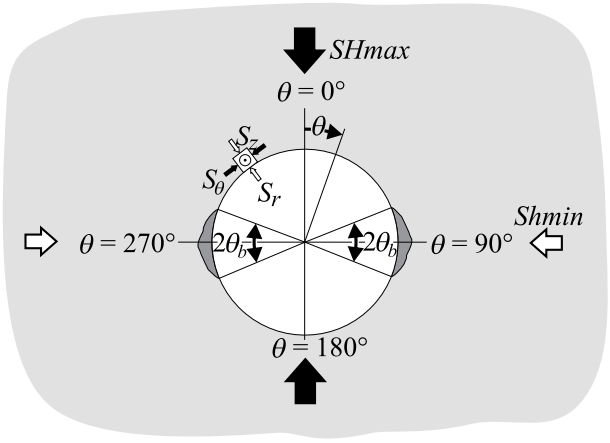

Fig. 3. Definition of the variables in a cylindrical borehole coordinate system aligned with a vertical well.

The question of which of the three principal stresses at the borehole wall correspond to the maximum, intermediate or minimum stress for any far field stress condition (i.e. any combination of *Shmin*, *SHmax*, *Sv* and *Pw*) and any location around the hole (θ) is not trivial. However, when considering the circumferential locations most favourable for breakout-failure (i.e. sectors centred at $\theta = 90$ or 270°), $S_\theta > S_z > S_r$ is valid in most situations. An exception arises when *SHmax* and *Shmin* are almost equal and of low magnitudes compared to *Sv*. In this situation, S_z can become the maximum principal stress. Special care must thus be taken when considering borehole failure analyses in such a stress regime. A similar situation occurs when considering the orientation at which DITFs can form (i.e. at $\theta = 0$ or 180°). Typically, for $\theta = 0°$ or 180°, $S_\theta < S_z$, although, there are some stress regimes for which this is not the case and transverse DITFs can occur.[37,38]

4.3. Failure criteria

In this section, we describe the various failure criteria applied in the analysis. Reviews of failure criteria used in wellbore failure analysis can be found in Colmenares and Zoback[39] and Zhang et al.[40] The criteria were parametrized to the case of the Basel monzogranite using data from a single multi-stage confined compression test performed on a core plug by Braun.[24] The 34 mm diameter sample was 70 mm in length, and was itself cored from the 100 mm diameter core recovered from the BS-1 hole. The sample was jacketed so that the confining fluid could not penetrate it. The sample is from a depth of 4902 m, and consists of monzogranite with a composition of approximately 50% quartz, 25% plagioclase, 10% potassium feldspar and 15% ferromagnesian minerals. The grain size in the plug sample is about 3–5 mm, although large K-feldspars (up to 5 cm long) are present in the BS1 core. It was tested under axial loading with increasing confinement in steps of 5, 10, 30, 50 and 70 MPa. Confinement was increased when non-linearity, considered as evidence of yield, was identified on the axial or radial strain records. The axial stress at yield for each of the confining stress levels are listed in Table 1. The elastic properties determined during the first loading step with 5 MPa confinement and ignoring initial closure effects are $E = 39$ GPa for the Young's modulus and $\nu = 0.22$ for the Poisson's ratio. Similar values were obtained in subsequent steps at higher confining pressure. The implied static Young's modulus is unrealistically low for a fine-grained monzogranite and is not consistent with the average dynamic modulus between 4896.5 m and 4906.5 m depth derived from sonic and density logs of 80 GPa with a standard deviation of 3.3 GPa (see Fig. 4). Static Young's modulus would be expected to be only 15–20% lower than dynamic modulus,[41] which in this case would be about 65 GPa, but not 50% less. A possible explanation for this discrepancy could be the presence of core damage, although in this case one would expect the effect of damage on modulus would diminished with increasing confinement, which is not observed. This discrepancy in modulus is currently unexplained. In view of the fact that only one multi-stage measurement was made, and the consistency of the dynamic modulus estimates, we use a Young's modulus of 65 GPa in the analyses. The coefficient of linear thermal expansion was estimated based on mineralogical composition following approaches described in.[42,43] Computing the thermal expansion coefficient of a mineral aggregate using a weighted arithmetic and harmonic average it was possible to bracket its value to be approximately 1e-5 K^{-1}.

Table 1
Results from multi-stage strength testing of a single plug from of the Basel core from Braun.[24]

$\sigma_2 = \sigma_3$ (confinement) [MPa]	5	10	30	50	70
σ_1 (axial load at estimated yield point) [MPa]	169.7	221.7	337.3	442.5	557.3

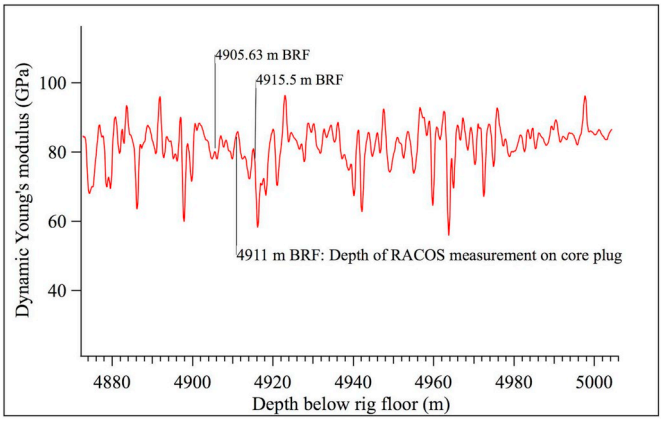

Fig. 4. Comparison of dynamic modulus profile in the vicinity of the static modulus determination by Braun.[24] The average dynamic Young's modulus in depth range 4905.63–4915.5 m BRF is 80 ± 3.3 GPa (4896.63–4906.5 mBG).

A number of factors must be born in mind when considering the degree to which the data in Table 1 reflect the strength characteristics of the intact rock under in-situ conditions. Significant core damage in the form of disking or incipient disking with 2–3 cm spacing was observed along the entire 10 m length of the 10 cm diameter core extracted from near the bottom of the BS-1 borehole. Although it is likely that the plug used in the strength testing was selected to be as far as possible from an incipient disking fracture, the spacing and ubiquitous nature of the incipient disking would make it difficult to find a zone to extract a 34 mm plug that did not contain significant microscopic damage associated with the disking process. In any case, relaxation of in-situ stress would induce microscopic damage that would serve to reduce the strength and Young's modulus of the sample, and increase its Poisson's ratio. Strength reductions due to stress relaxation of up to 30% have been reported,[30] and disking-related damage would add to this. Moreover, the size of the sample tested is significantly smaller than recommended,[44] although this is more likely to have the opposite effect of producing an overestimate of the strength and modulus compared to tests on standard size samples.[45] A further concern is that the multistage procedure used in the testing can generate bias if the loading system is too slow to react to the onset of yield and significant damage occurs before the sample is stabilized by increasing the confinement. If such occurs, the strength estimate at higher confinement tends to be low, leading to underestimation of the internal friction angle. Finally, only a single test was performed, and thus there is no demonstration of reproducibility or assessment of the variability of strength characteristics along the hole. In view of these limitations, the strength estimates given in Table 1 are taken as tentative, and it is acknowledged that the degree to which they represent the strength characteristics of the rock along the borehole is questionable. In addition, some authors[7,46] have reported reduced strength for test performed on very low permeability rock in conditions were the confining fluid was allowed to penetrate the sample. Specifically, they found that the onset of dilation allowed the confining fluid to penetrate the sample, leading to sudden failure at stress levels 50%–70% lower than measured on dry jacketed samples of the same rock type. They claimed that these failure conditions are more representative of the wellbore conditions when breakouts forms. In the case of the Basel well, the natural pore pressure and the borehole fluid pressure are in quasi-equilibrium, which is why we take $Pw = Pp$. With the pore pressure being pervasive throughout the rock and the wellbore pressure being in equilibrium with the pore pressure, there isn't any direct reason for a sudden penetration of wellbore fluid into newly formed cracks at the onset of dilation. One could even argue that the volume increase related to the onset of dilation would induce actually a pore pressure drop leading to an effective strengthening of the material. Nevertheless, we considered such potential effects in a sensitivity study presented in Appendix where the failure criteria are parametrized with peak strength reduced to up to 55% of the reported peak strength.

For all failure criteria considered, the weakening effect of pore pressure as described by an effective stress law must be included. The effective stresses, σ are computed from total stress, S, as:

$$\sigma = S - \beta Pp \tag{10}$$

where $0 \leq \beta \leq 1$ is a coefficient in the effective stress law that depends of the failure mode. For compressive failure we consider a coefficient $\beta_c = 1.0$, as found by Brace and Martin[47] to be valid for low-porosity crystalline rocks. For the tensile failure of low porosity crystalline rocks, the value of β_t remains controversial.[8,48–52] In order to deal with this uncertainty, we will consider the two extreme scenarios with $\beta_t = 1.0$ and $\beta_t = 0.0$, respectively.

In the following, several strength criteria for compressive failure (i.e. Rankine, Mohr-Coulomb, Mogi-Coulomb and Hoek-Brown) and one for tensile failure are parametrized using the multi-stage measurements on the Basel monzodiorite core plug listed in Table 1.

4.3.1. Rankine criterion

This is the simplest of the compressive failure criteria in which the strength of the borehole wall is assumed to be a constant, independent of the intermediate or minimum effective stresses, σ_2 or σ_3. With this criterion, failure occurs when the maximum effective principal stress, σ_1, exceeds a strength threshold, C_o^R. That is,

$$\sigma_1 \geq C_o^R \tag{11}$$

The strength threshold C_o^R is usually taken as equal to the uniaxial compressive strength, although some authors suggest that it can be significantly less. For example, Walton et al.[53] consider the wall strength to be about 75% of the uniaxial compressive strength. The value of the uniaxial compressive strength for the Basel granite is discussed below.

4.3.2. Mohr-Coulomb criterion

In the Mohr-Coulomb criterion, rock strength increases linearly with the minimum effective principal stress. This criterion can be expressed in terms of effective principal stresses as:

$$\sigma_1 \geq C_o + q\sigma_3 \tag{12}$$

where C_o is the uniaxial compressive strength, and q is a material constant that can be related to the internal friction angle, ϕ, through $q = tan^2\left(\frac{\pi}{4} + \frac{\phi}{2}\right)$. The internal friction angle, ϕ, relates to the coefficient of internal friction, μ, through $\mu = \tan(\phi)$. Plots of the Mohr-Coulomb criterion in $(\sigma_3 - \sigma_1)$ and $(\sigma_n - \tau)$ spaces for the Basel data given in Table 1 are shown in Fig. 5. The data follow linear trends except for the

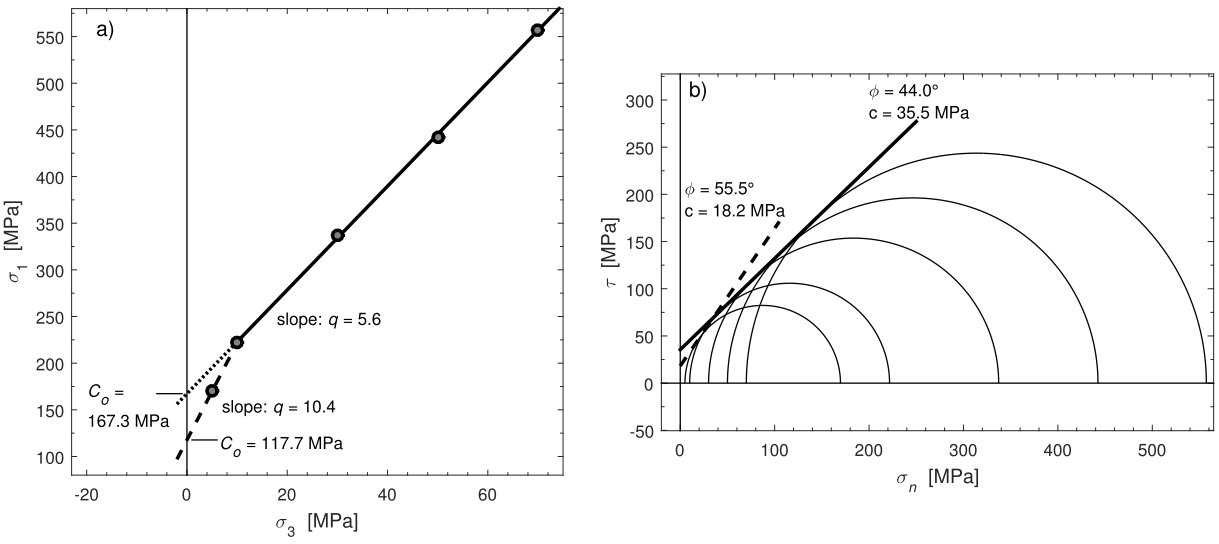

Fig. 5. Strength data of Table 1 for the Basel granite with best linear fits in a) $\sigma_3 - \sigma_1$ and b) $\sigma_n - \tau$ spaces.

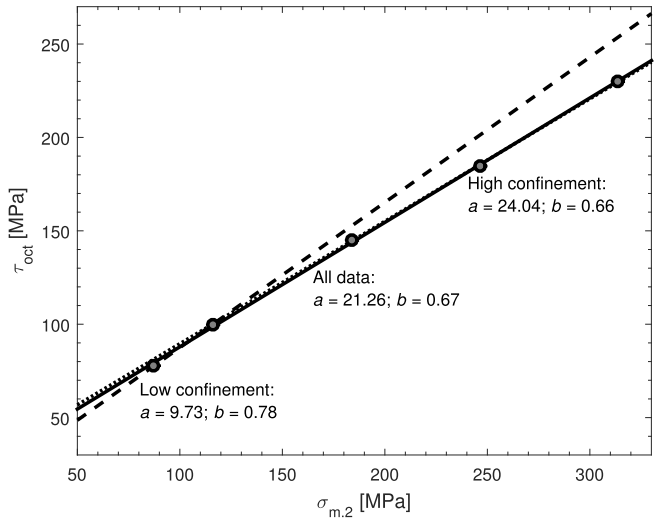

Fig. 6. Strength data of Table 1 for the Basel granite plotted in $\sigma_{m.2} - \tau_{oct}$ space (circles). See text for description of the linear fits.

data point at the lowest confining pressure of 5 MPa which indicates a lower σ_1 failure stress. Taken on face value, this suggests either a curved criterion (e.g. the Hoek-Brown criterion discussed shortly) or a bilinear criterion. However, the possibility that it reflects sample damage cannot be ruled out. If one discards the 5 MPa confinement data point, the extrapolated strength at zero confinement (i.e. the uniaxial compressive strength) is $C_o = 167$ MPa (dotted line on Fig. 5a), and the internal friction angle is 44°. However, if the lowermost data point is considered valid, then the linear fit through the two lowermost confinement data points (dashed line on Fig. 5a) or a curved criterion through all data, gives $C_o = 118MPa$. The implied internal friction angles are 55.5° for confinement smaller than 10 MPa, and 44.0° for confinement higher than 10 MPa (Fig. 5b). In the stress calculations, we will use C_o values of 118 and 167 MPa to bracket the range of values. Such values are in the correct range for large grainsize granitic to granodioritic rocks published in the literature.[54]

4.3.3. Mogi-Coulomb criterion

The Mogi-Coulomb criterion, proposed by Al-Ajmi and Zimmerman[55] is a linearized version of Mogi's criterion[56] that relates the octahedral shear stress, $\tau_{oct} = \frac{1}{3}\sqrt{(\sigma_1 - \sigma_2)^2 + (\sigma_2 - \sigma_3)^2 + (\sigma_3 - \sigma_1)^2}$ to the mean stress, $\sigma_{m.2} = \frac{\sigma_1 + \sigma_3}{2}$. Expressed in $\sigma_{m.2} - \tau_{oct}$ space, the failure criterion is:

$$\tau_{oct} \geq a + b\sigma_{m.2} \tag{13}$$

The parameters a and b are material constants that are related the Mohr-Coulomb parameters of internal friction, ϕ, and cohesion, c, by $a = \frac{2\sqrt{2}}{3} c\ cos(\phi)$ and $b = \frac{2\sqrt{2}}{3} sin(\phi)$. The strength test data from Table 1 are plotted in $\sigma_{m.2} - \tau_{oct}$ space in Fig. 6. The solid black line denotes the best linear fit to all the test data points (circles). Also shown are the two failure lines derived from the Mohr-Coulomb parameters given in Fig. 5: the dashed line denotes the fit to the two low-confinement data, and the dotted line denotes the fit to all points except the lowest confinement point (referred as High confinement in Fig. 6). The latter is essentially identical to the fit on all data.

4.3.4. Three dimensional Hoek-Brown criterion

The Hoek-Brown failure criterion[54] is an empirical, non-linear failure criterion that is based upon empirical[57] and theoretical considerations.[58] For intact rock, it has the form:

$$\sigma_1 \geq \sigma_3 + C_o\sqrt{m_i\frac{\sigma_3}{C_o} + 1} \tag{14}$$

where mi and C_0 are the strength parameters. The strength data from Table 1 are plotted in $(\sigma_3 - \sigma_1)$ space in Fig. 7a, together with the best-fitting curve of the form of Eq. (14). Zhang and Zhu[59] proposed an extension of this criterion in order to account for the intermediate principal stress. Expressed in $\sigma_{m.2} - \tau_{oct}$ space, it takes the form:

$$\frac{9}{2C_o}\tau_{oct}^2 + \frac{3}{2\sqrt{2}}m_i\tau_{oct} - m_i\sigma_{m.2} \geq C_o \tag{15}$$

and can be understood as a non-linear version of the Mogi criterion. The data from Table 1 are plotted in $(\sigma_{m.2} - \tau_{oct})$ space in Fig. 7b. The fitted curve is obtained by introducing the parameters C_o and m_i determined in $(\sigma_3 - \sigma_1)$ space (Eq. (14)) in Eq. (15) and this produces a very satisfactory fit. A least square best fit to the data directly in the $(\sigma_{m.2} - \tau_{oct})$ space leads to only slightly different fitting parameters. The strength parameters values obtained of $C_o = 109MPa$ and $m_i = 27.7$, are in agreement with published values for such rock type,[54] although C_o is on the lower end of the range of expected values.

4.3.5. Tensile strength

For tensile failure, a simple failure criterion of the Rankine type is adopted. Specifically,

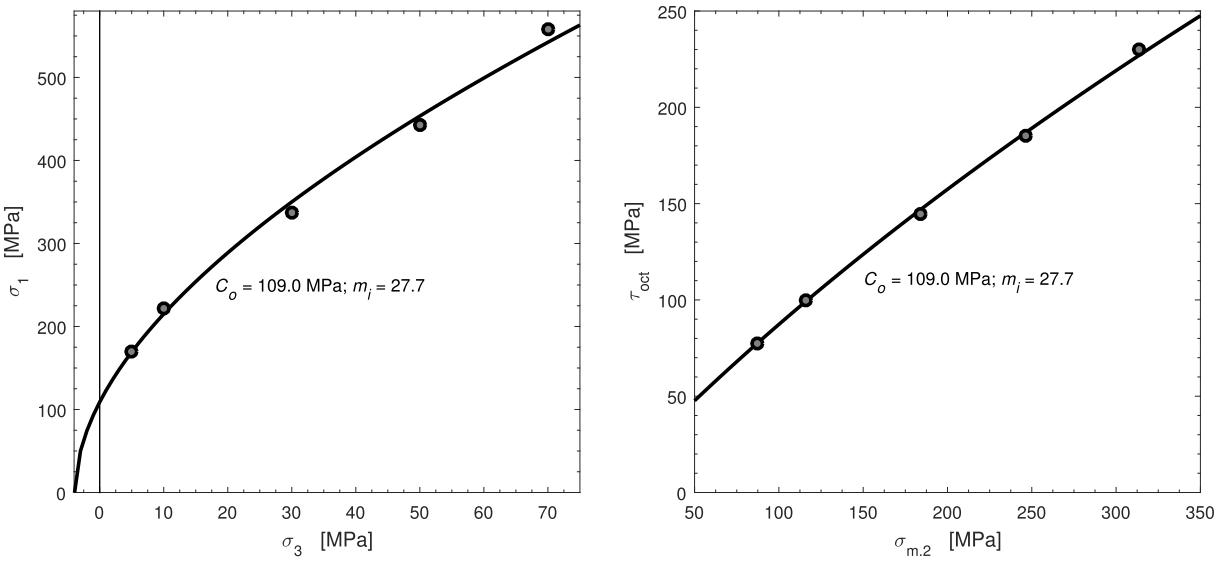

Fig. 7. a) Hoek-Brown criterion fit through the Basel core-test strength data in ($\sigma_3 - \sigma_1$) space. b) Same data and same fit in ($\sigma_{m.2} - \tau_{oct}$) space.

$$\sigma_3 \leq -T \tag{16}$$

where σ_3 is the minimum effective stress at the borehole wall and T is the tensile strength.

The tensile strength of the Basel granite has not been measured. Following the approach of Perras and Diederichs,[60] the tensile strength will be approximated using the parameters of the Hoek-Brown failure criteria[54] with the following relationship:

$$T = \frac{C_o}{m_i} \tag{17}$$

where C_o is the uniaxial compressive strength and m_i is the frictional parameter in the Hoek-Brown relation. Using the Hoek-Brown parameters derived above in Eq. (17) leads to an estimate for T of 4 MPa. This is slightly less than expected values for the rock type[60] and could be influenced by the relatively low C_o determined above. Assuming that the strength data at the lowest confining pressures is affected by sample damage, and that this should be ignored in the determination of C_o (i.e. C_o should be taken 167.3 MPa in Fig. 5), then the tensile strength estimate increases to $T = 6$ MPa. In practice, the tensile strength of the borehole wall is often taken as 0 MPa, a view justified by the likelihood that a cohesionless flaw will be present at the borehole wall to initiate tensile failure. Neglecting the tensile strength of the borehole wall does not greatly add to the uncertainty of the analysis.

4.4. SHmax estimate from breakout width

An expression relating stress magnitudes to breakout width was given by Barton et al.[29] using a Rankine failure criterion. Specifically, they assumed that the width of a breakout that formed for a given combination of far-field stresses, *SHmax* and *Shmin*, and interval wellbore pressure, *Pw*, would be defined by all points around the borehole wall where the effective tangent stress, $\sigma_\theta = S_\theta - P_p$ (assuming $\beta_c = 1.0$), reaches or exceeds the Rankine failure threshold, C_o^R. They derived an equation for computing *SHmax* from breakout half width, θ_b, given an independent estimate for *Shmin* was available. After modification to include the presence of a thermal component, $S_\theta^{\Delta T}$ (Eq. (9)) to the tangent stress at the wellbore wall arising from a possible temperature perturbation from ambient,[61] the relation becomes:

$$SHmax = \frac{C_o^R + Pp + Pw - S_\theta^{\Delta T} - Shmin(1 - 2cos(2\theta_b))}{1 + 2cos(2\theta_b)} \tag{18}$$

This approach makes several questionable assumptions. Firstly, the effect of evolving borehole geometry on the tangent stress at the borehole wall during breakout development is not considered. The validity of this simplification is not clear and may depend of the mode of failure. Secondly, it is assumed that S_θ is the maximum principal stress for all values of θ, which is not always strictly the case. As discussed in Section 4.2, this assumption is almost always true for $\theta = 90$ and 270°, but is often not true for $\theta = 0$ and 180°. Eq. (18) is thus not valid for very wide breakouts. Another reason why Eq. (18) is not valid for wide breakouts is due to its asymptotic behaviour: as breakout width, $2\theta_b$ approaches 120°, the denominator of Eq. (18) approaches zero and thus *SHmax* becomes undetermined. Moreover, for widths close to 120°, small variations in width produce large changes in the estimate of *SHmax*, leading to poor constraints on *SHmax*. For these two reasons, the use of Eq. (18) is not recommended when the breakout width is larger than 100°.

A slightly different expression can be derived using a Mohr-Coulomb criterion (Eq. (12)), where strength is a function of the minimum effective principal stress, σ_3. Here, the maximum principal stress is taken as S_θ (Eq. (6)) and the minimum principal stress as S_r (Eq. (5)). The estimate of *SHmax* is obtained in the same manner as for the Rankine criterion by solving for *SHmax* at the breakout edge, which is given by:

$$SHmax = \frac{C_o + Pp + Pw - S_\theta^{\Delta T} - Ppq + Pwq - Shmin(1 - 2cos(2\theta_b))}{1 + 2cos(2\theta_b)} \tag{19}$$

where q is the frictional strength component as defined in Eq. (12). This relation suffers from the same limitations as Eq. (5) and should not be used for breakout width larger than 100°. It is important to note that Eq. (19) reduces to Eq. (18) when $Pw = Pp$, because then the minimum effective principal stress at the borehole wall becomes zero, and the borehole wall strength is then constant and equal to C_o. In our analyses, we take $Pw = Pp$, and so the results for the Mohr-Coulomb criterion are identical to the Rankine criterion, with, $C_o^R = C_o$.

Analytical solutions for *SHmax* are not easily derived when considering criteria where the intermediate effective principal stress, σ_2, influences the strength (e.g. Mogi-Coulomb or Hoek-Brown 3D). However, the solution can be computed numerically. In addition, when computing the solution numerically, the relative magnitudes of S_θ,S_z and S_r can be checked before introducing them into the failure criterion, which removes one of the limitations discussed above.

The *SHmax-Shmin* solution spaces obtained from numerical computations of the breakout width using each the four failure criteria parameterized using the data in Table 1 are presented in Fig. 8 for

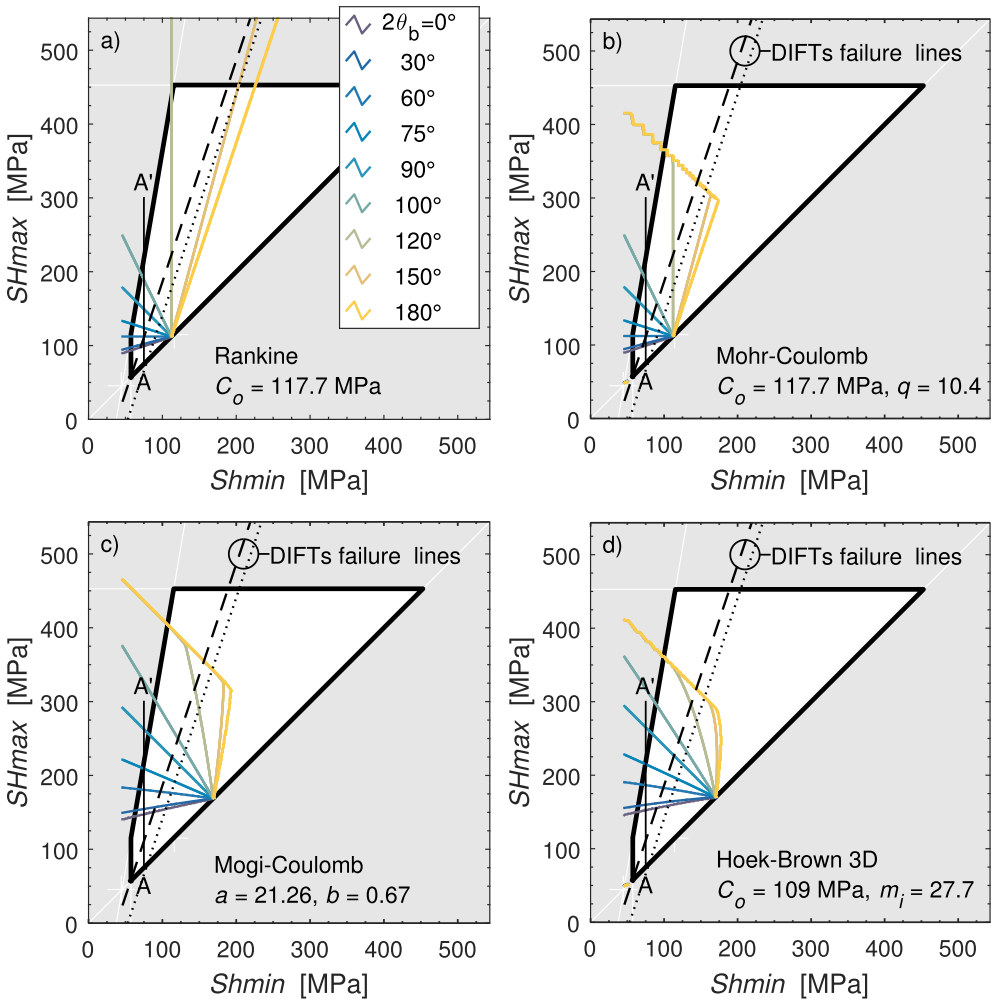

Fig. 8. *SHmax-Shmin* solution space at the top of the open hole section (4632 m depth BG) for a range of breakout widths ($2\theta_b$) obtained numerically for the following failure criteria parameterized by the strength characteristics measured on the plug from the Basel-1 core: a) Rankine criterion, b) Mohr-Coulomb criterion, c) Mogi-Coulomb criterion and d) Hoek-Brown 3D criterion. The assumed parameter values at 4632 m are: Sv = 115 MPa, $Pp = Pw$ = 45 MPa. A thermal stress of - 15.8 MPa is included to reflect a persisting 19 °C cooling of the hole after drilling and a Poisson's ratio of 0.22 is assumed. The bold lines denote limits on *SHmax* imposed by assuming that crustal strength is limited by a Coulomb friction criterion with a friction coefficient of 1.0. Dotted and dashed black lines are DITFs failure lines (see Section 4.5, Eq. (3)) for a tensile strength of 4 MPa and a coefficient for effective stress law β_t of 1.0 or 0.0, respectively. These also include the effect of a prevailing thermal stress of – 72.5 MPa arising from the estimated 87 °C cooling experienced by the lower reaches of the borehole during drilling (see Section 4.6).

vertical stress and pore/wellbore pressure values appropriate for a depth of 4632 m BG. Curves are shown for a range of breakout widths. For the Rankine and Mohr-Coulomb analyses, we used the low confinement uniaxial compressive strength and frictional parameters derived in Section 4.3.2, although later in this paper, both parametrisations will be evaluated. The Rankine and Mohr-Coulomb criteria lead to identical results except at very high *SHmax* magnitudes. This is due to the fact that with very high *SHmax* magnitudes, the minimum principal stress at the borehole wall required for wide breakout failure becomes the axial component (S_Z) and is negative. With the Mohr-Coulomb criteria, a negative minimum principal stress leads to a weakening of the borehole wall to values less than, C_0 [62–64] an effect which is not captured by the Rankine criteria. Such low axial effective stress component can, however, lead to transverse fractures.[37] This effect is not captured by Eq. (6), which assumes that the minimum principal stress is always the radial stress and is never negative. The contour line for 120° breakout width is vertical, indicating complete insensitivity to *SHmax* which reflects the asymptotic behaviour of Eqs. (5) and (6). For the true triaxial criteria (Mogi-Coulomb and Hoek-Brown 3D), the effect of the intermediate stress is to translate the initiation of failure (0° breakout width contour) to a higher SHmax magnitude compared to the Mohr-Coulomb case.

Fig. 9 shows the dependence of breakout width on *SHmax* magnitude for the case *Shmin* = 75 MPa, which corresponds to the estimated conditions at the top of the open-hole in the Basel reservoir. For the Mogi-Coulomb and Hoek-Brown 3D criteria, failure initiates for *SHmax* magnitudes of 147 MPa and 151 MPa respectively, whereas for the Rankine and Mohr Coulomb criteria initiation occurs at an SHmax level of 99 MPa, which is 48–52 MPa lower. At a breakout width of 95°, the predicted *SHmax* difference for the two pairs of criteria increases to about 125 MPa. The curves of Fig. 9 are very steep at breakout initiation which means that a subsequent small increase in *SHmax* of only 2.5 MPa results in a 20° increase in predicted breakout width (true for all criteria). This suggests that breakout widths less than 20° are not stable, in agreement with the fact that such narrow breakouts are rarely observed.

The curves of Fig. 9 also show that if *Shmin* and the breakout width are known, the magnitude of *SHmax* can be uniquely determined for a given failure criterion, at least for breakout widths in the range 0°–100°, either using Eqs. (18) and (19) or by numerically searching for the matching *SHmax* magnitude. Later, this approach will be applied to the profile of breakout widths in the BS-1 well to obtain profiles of *SHmax*.

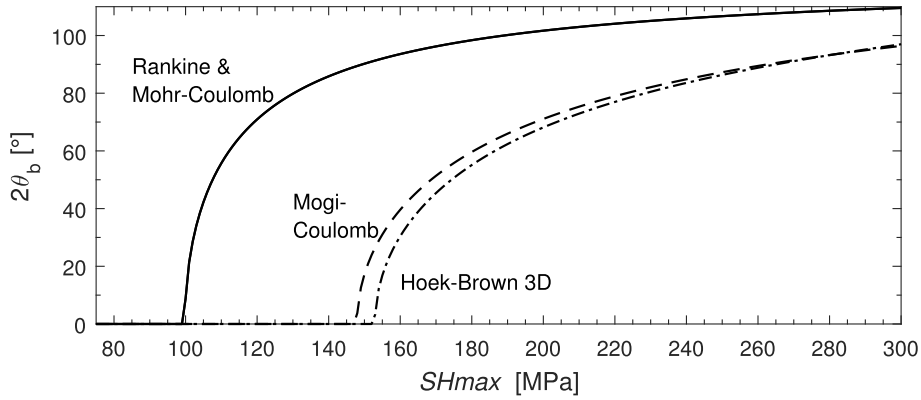

Fig. 9. Breakout width as a function of *SHmax* for the four strength criteria parameterized with the strength data from Table 1. A value for *Shmin* of 75 MPa was used, as appropriate for the top of the open hole section of the Basel reservoir. The curves define the combinations of *SHmax* and breakout widths prevailing along profiles A-A′ in Fig. 8 a) to d).

4.5. Constraints on SHmax from DITFs

The observation of DITFs at a given depth allows further constraints on *SHmax* to be imposed by considering the stress conditions required for tensile failure at the borehole wall for $\theta = 0$ or 180° (Eq. (6)), using the tensile failure criterion given by Eq. (16), and an appropriate effective stress law (Eq. (10)). Specifically, the observation of DITFs implies the following inequality is satisfied:

$$SHmax \geq 3Shmin - Pw + S^{\theta}_{\Delta T} - \beta_t Pp + T \quad (20)$$

If *Shmin* and other stress components of Eq. (20) are known, then Eq. (20) can be used to compute a lower bound on *SHmax*. If *Shmin* is not known, then Eq. (20) can be used to plot pairs of values in *Shmin* – *SHmax* space which are consistent with DITF formation. The coincident observation of breakouts and DITFs places relatively strong constraints both stress magnitude estimates. This is evident in Fig. 8 where the tensile failure lines for $\beta_t = 0.0$ and 1.0 are plotted in *Shmin* – *SHmax* space for the top of the open hole section (4632 m depth BG) together with *Shmin* – *SHmax* contours for various breakout widths. For the DITF failure lines, acceptable *Shmin* – *SHmax* pairs of values lies to the left of the line. Note that this is a hypothetical example as neither borehole breakouts nor DITFs are observed at the depth of 4632 m considered in the figure. As is clear from Eqs. (18)–(20), a thermo-elastic stress component, $S^{\Delta T}_{\theta}$, arising from cooling of the borehole wall, has a direct impact on the constraints on *SHmax* imposed by presence of breakouts and/or DITFs. It is thus of considerable importance to correctly estimate the temperature deviations from ambient at the times relevant to the two forms of failure. This is discussed in the following section.

4.6. Temperature perturbation estimation

In order to estimate the thermal stresses prevailing around the borehole at the times of failure, it is necessary to reconstitute some characteristics of the borehole thermal history based on available data. A mud cooler was used during drilling and the mud was typically re-injected at a temperature of 40–55 °C. After completing drilling to a total depth of 5000 m, the mud circulation was stopped on 22-Oct-2006. The UBI log used to determine the presence of borehole failure (Fig. 2a – b) was obtained four days later on the 27-Oct-2006. The maximum temperature recorded within the sonde during the UBI logging was 158 °C. Two calibrated temperature logs were acquired prior to UBI logging: one on the 23-Oct-2006, 20.3 h after end of circulation, and one on the 24-Oct-2006, 51.5 h after end of circulation. Both temperature logs are presented in Fig. 10a as grey and black dashed lines, respectively. One temperature log was run to 4.6 km more than two years after drilling completion, on 10-Dec-2008, and is taken to be representative of the in-situ conditions without the drilling-induced temperature perturbation (Fig. 10a, black solid line).

Temperature measurements were also acquired by Electronic Multishot Surveys (EMS), details of which are given in the Appendix. The EMS data give bottom hole temperatures during pauses in drilling at 4429 m, 4687 m and 4988 m depth of 84 °C, 83.5 °C and 89 °C respectively.

For the analysis of breakout width, the temperature perturbation of relevance is the drawdown in temperature from the natural conditions that is persisting at the time the breakout width is measured (i.e. the time of the UBI log). As cooling during circulation ended on 23-Oct-2006 and the UBI log was run four days later, the well was still heating up at that time, and thus further increases in breakout width can be anticipated in response to increasing thermo-elastic hoop stress.[65] The bottom-hole temperature history after stopping circulation has been analysed using the Horner method in order to assess the bottom hole temperature when the UBI logs were acquired (27-Oct-2006). The estimated bottom hole temperature is in the range 172–177 °C, which is 5–10 °C higher than the bottom hole temperature recorded with the complete temperature profile of 24-Oct-2006. The temperature while logging is thus estimated by offsetting the 24-Oct-2006 log by 5–10 °C resulting in the dark grey temperature range displayed in Fig. 10a. Taking the log of 10-Dec-2008 log as representative of natural formation temperature, the residual cooling relevant for the borehole breakout analysis is greatest at 4735 m, where it is 17–22 °C (see Fig. 10b). The residual cooling is slightly less at the bottom hole (9–14 °C) and it progressively decreases above 4 km depth to reach 5–10 °C at 2500 m. For the thermo-elastic properties of the Basel monzodiorite (see Section 4.3), the corresponding thermo-elastic hoop stress contributions are −14 to −18 MPa at 4735 m depth, −8 to −12 MPa at the bottom hole, and −4 to −8 MPa at 2500 m.

For the formation of DITFs at a given depth, the important temperature change is the largest amount of cooling that the borehole at that depth experienced during drilling. Thus, the analysis requires the estimation of the profile of maximum cooling. Under most circumstances, the greatest cooling occurs near the bit where relatively cool mud emerging from the bit contacts the rock. The maximum cooling profile can be determined if mud temperature is measured in the bottom-hole-assembly with measurement-while-drilling technology. Unfortunately, no MWD system was employed in the BS-1 well. A firm lower bound on the maximum cooling profile is set by the temperature log from 23-Oct-2006 which was run 20 h after the circulation was stopped. This log suggests cooling up to almost 40 °C (corresponding to a hoop stress of −33 MPa). However, the maximum cooling is likely to be significantly greater than this. The temperature profiles collected with the EMS logs indicate bottom-hole cooling of up to 100 °C (see

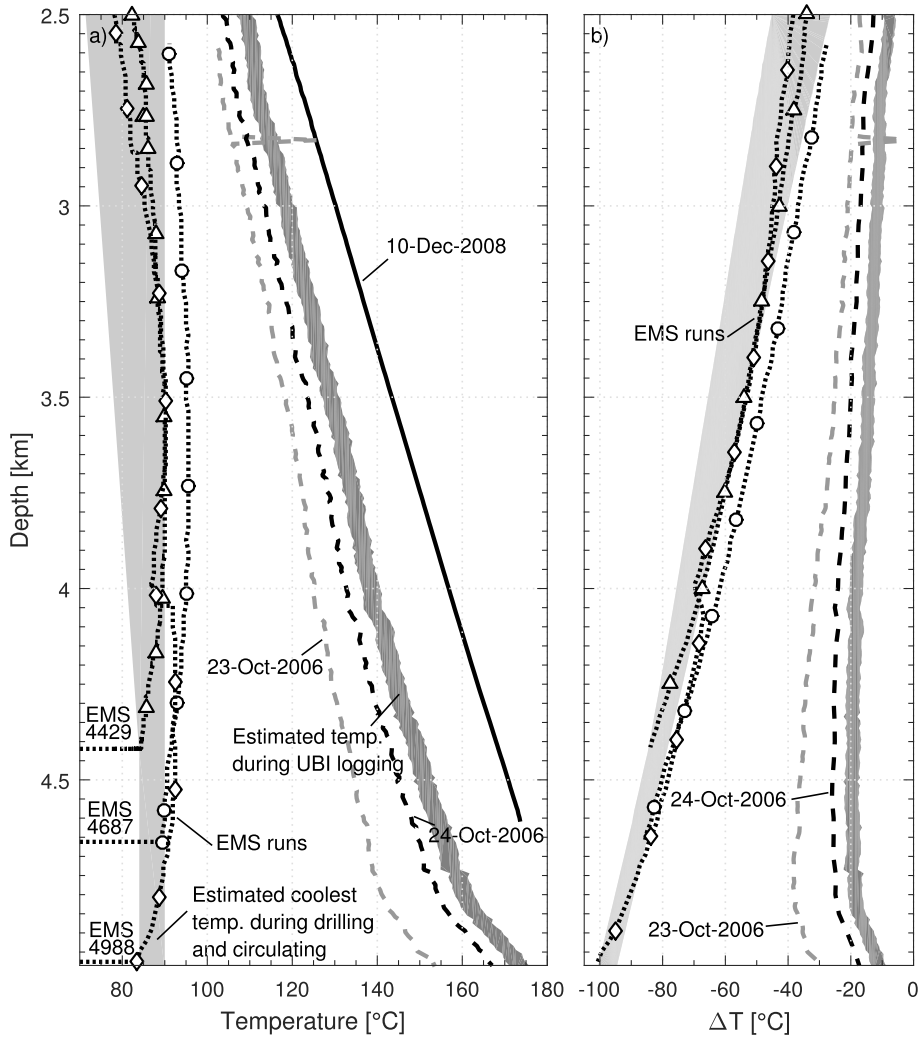

Fig. 10. a) Temperature logs acquired in BS-1 at different dates (see text for details). b) Cooling, ΔT, of the wellbore computed from the difference between the temperature logs and the reference log of the 10-Dec-2008. Since the latter was only acquired down to 4600 m, it was linearly extrapolated to greater depth. The temperature during UBI logging (dark grey area) is estimated using the Horner method that indicates that the bottom temperature was about 5–10 °C higher than during the acquisition of the 24-Oct log.

Fig. 10b) implying very high thermal hoop stresses up to −83 MPa. The EMS data, whilst limited by the fact that they are essentially point measurements that are few in number, nevertheless provide reasonable estimates of the amount of cooling that prevailed at the hole bottom during drilling. Thus, they were used to determine the cooling and hence the thermo-elastic stress for the DITF analyses. The profile of maximum cooling used in our analyses, which is shown by the light grey area in Fig. 10, passes through the three EMS data points, and was extrapolated to the surface so as to respect the average temperature of the mud returns on surface during circulation of about 55 °C. Clearly, the uncertainty of the profile is less in the lower part of the hole where EMS data are available than in the upper part of the well where no data are present. The profile of the amount of cooling from the ambient temperature is derived from the maximum-cooling profile by subtracting the profile of natural formation temperature given by the log from 10-Dec-2010. The amount of cooling is maximum at the bottom hole where it ranges from 94 to 100 °C corresponding to a thermally induced hoop stress of 78–83 MPa. At 2500 m depth, the cooling is about 27–45 °C, corresponding to a hoop stress of 23–38 MPa.

4.7. Constraints on SHmax from breakout width

The breakout width profile shown in Fig. 2d was used to determine a profile of *SHmax* assuming the profiles of *Sv* and *Shmin* are given by Eqs. (1) and (2) respectively. A thermal stress component of $S_\theta^{\Delta T} = S_z^{\Delta T}$ was computed using the cooling profile in Fig. 10b (dark grey area). The four different compressive failure criteria described in Section 4.3 were considered in the analysis. The magnitude of *SHmax* at each depth was derived numerically by solving the forward problem (i.e. computing the expected breakout width) by iteratively adjusting the *SHmax* value until a good match with the observed breakout width was found. A minimization routine by Forsythe et al.[66] that is implemented in the MATLAB™ Optimization Toolbox was used. When the observed breakout width exceeded about 100° (i.e. getting close to the asymptote at 120° mentioned in Section 4.4), a sensible match could not be achieved and thus no solution was obtained. At depths where no breakouts were observed, the computed *SHmax* level for breakout initiation was taken as an upper bound for *SHmax*. The *SHmax* profiles resulting from these computations for the four failure criteria are presented on Fig. 11a–d, together with bounds on *SHmax* imposed by assuming that crustal strength is limited by a Coulomb friction criterion with friction coefficients, μ, of 0.6 and 1.0.

A common, and somewhat surprising feature of all the computed *SHmax* profiles is the very low or slightly negative gradient with depth. The best-fitting linear depth trends to the four *SHmax* profiles have gradients of −2 MPa/km and −6 MPa/km for the Mohr-Coulomb/

Rankine criteria with uniaxial compressive strengths of 118 and 167 MPa respectively (Fig. 11a and b), −3 MPa/km for the Mogi-Coulomb criterion (Fig. 11c), and 4 MPa/km for the Hoek-Brown 3D criterion (Fig. 11d). A reduction in the strength estimate due to possible pore pressure effects does not significantly affect these gradients, as shown in the sensitivity analyses presented in Fig. A-3 in Appendix. Such low *SHmax* gradients are a consequence of the observation that breakout width decreases with depth. The *SHmax* trends are dependent to some degree on the *Shmin* profile assumed in the computation. This is given by Eq. (2), and was constrained by a single datapoint given by the limiting pressure observed at the casing shoe during stimulation. An independent estimate of *Shmin* can be derived by a stress computation that takes into account both breakouts and DITFs. This approach is taken in the next section to give further insights on the validity of the results presented in Fig. 11.

4.8. Additional constraints from DITFs

When both compressive failure criteria (Eqs. (11)–(13), or 15) and tensile failure criteria (Eq. (16)) are considered simultaneously, constraints on both *Shmin* and *SHmax* can be computed. An example of such a computation is given in Fig. 12 for the depth range 4298–4308 m BG, where both breakouts and DITFs occur together (see the acoustic amplitude image of Fig. 12a). The observed breakout width over this section of 60°–80° and the presence of a pair of DITF failure traces can be used to resolve both stress magnitudes in the *Shmin* - *SHmax* diagram for this depth shown in Fig. 12b. Acceptable values of *Shmin* and *SHmax* for the case $\beta_i = 1.0$ are denoted by the shaded area lying to the left of the $\beta_i = 1.0$ failure line, with *Shmin* spanning the range 54–88 MPa and *SHmax* spanning the range 109–134 MPa (see caption of Fig. 12 for explanation). The *Shmin* magnitude range is consistent with the estimate of 69.3 MPa obtained from Eq. (2) at 4312 m depth. Since the vertical stress magnitude at this depth is estimated to be *Sv* = 107 MPa, the analysis implies a strike-slip regime at this depth.

The principle of the approach illustrated in Fig. 12 can be used to constrain stress at other depths by considering the constraints placed on the solution space by the presence or absence of breakouts and DITFs, as illustrated in Fig. 13. For the sake of simplicity, it is assumed that the coefficient in the effective stress law for tensile failure, β = 1.0, and the breakout width is assumed to be 80–90°. For the case where both breakouts and DITFs occur together, stress magnitudes that are consistent with the observed failure are limited to a polygon denoted by the dark grey area in Fig. 13a. If the breakout width is well resolved and takes a single value, the dark grey polygon collapses onto a line, but this still imposes bounds on both *Shmin* and *SHmax*. The other cases shown in the figure correspond to the presence of breakouts and absence of DITFs (Fig. 13b), the absence of breakouts and the presence of DITFs (Fig. 13c) and the simultaneous absence of both breakouts and DITFs (Fig. 13d). These cases are treated similarly, and all place constraints on admissible *Shmin* and *SHmax* magnitudes. Note the presence of two key points that often control the limits on the possible range of *Shmin* and *SHmax* magnitude. The first, denoted by the circle in Fig. 13, lies at the intersection of the SHmax = Shmin line with the lower bound on stress magnitude imposed by the assumed frictional strength of the crust (here

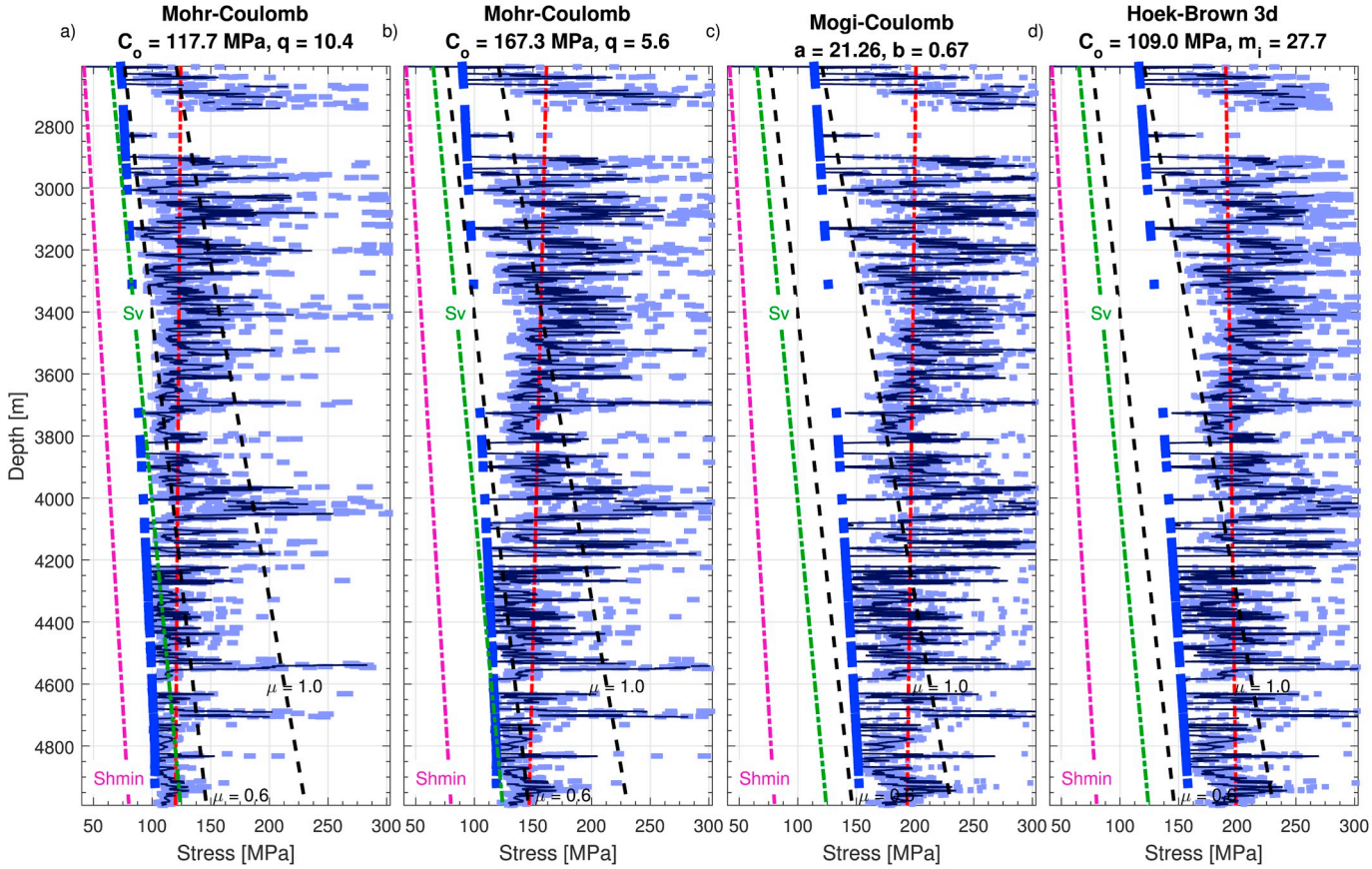

Fig. 11. *SHmax* estimates derived from breakout width for the four failure criteria considered and assuming the *Shmin* profile as given by Eq. (2): a) low confinement Mohr-Coulomb/Rankine with $\mathbf{C_o^R} = \mathbf{C_o}$ = 117.7 MPa; b) high confinement Mohr-Coulomb with $\mathbf{C_o^R} = \mathbf{C_o}$ = 167.3 MPa; c) Mogi-Coulomb (a = 21.26, b = 0.67); and d) Hoek-Brown 3D ($\mathbf{C_o}$ = 109.0MPa,$\mathbf{m_i}$ = 5.6). The Mohr-Coulomb and Rankine criteria are identical because *Pw* = *Pp*. Light blue horizontal markers: results of each individual *SHmax* computation, the horizontal range stemming from the uncertainty on the thermal stress solely. Solid black line: filtered result using a 7-points (2.8 m) moving average. Thick blue line: upper bound on *SHmax* computed at locations where no breakouts were observed. Black dashed lines: limits on *SHmax* imposed by assuming the crust strength is limited by a Coulomb friction criterion with friction coefficients, μ, of 0.6 and 1.0. Pink and green dashed lines: *Shmin* and *Sv*, respectively. Red dashed line: linear trend through the *SHmax* estimates.

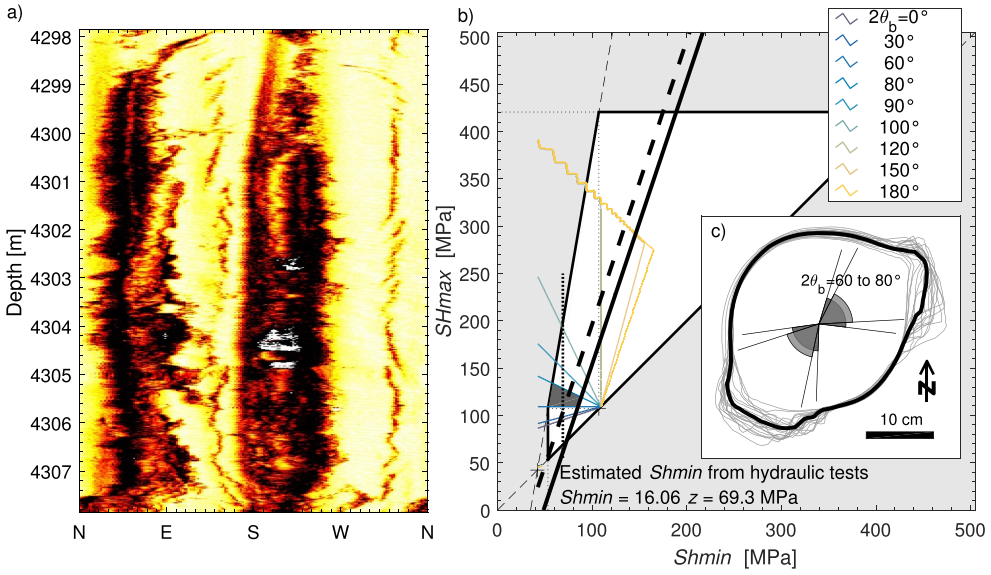

Fig. 12. a) Acoustic reflectivity image in the depth range 4298–4308 m BG which shows the presence of both breakouts and drilling induced tension fractures b) Constraints on the values of *SHmax* and *Shmin* that are consistent with breakout widths of 60–80° and the presence of DITF failure (see Section 4.4 for more details on this computation). Acceptable pairs of values are denoted by the dark shaded area. The *SHmax* computations for the breakouts assume a Mohr-Coulomb strength criteria with C_o = 117.7 MPa and q = 10.4 (see Fig. 5), and a cooling of the borehole wall of 19.6 °C implying the presence of a thermally induced hoop stress of 16.3 MPa. The computations for the DITFs assume a cooling of the borehole wall of 78.8 °C, giving a thermally induced hoop stress of 65.7 MPa. The stress polygon is computed assuming the rock mass has a Coulomb friction strength with a friction coefficient of μ = 1.0. The Vertical stress magnitude estimated form density log integration is for this depth 107 MPa. c) Borehole cross-section computed from acoustic transit time data averaged over the interval 4298–4308 m (thick black line) and over 40 cm subintervals within this depth range (thin grey lines). The estimated breakout with range from 60 to 80° is also indicated.

we assume μ = 1.0). The lower bound is computed from:

$$\frac{Sv - Pp}{\left[\sqrt{\mu^2 + 1} + \mu\right]^2} + Pp \tag{21}$$

The second key point, denoted by the square, is the breakout width singularity point where all breakouts width contours converge on the *Shmin* = *SHmax* limit of the stress polygon. When the stress state is isotropic in the plane perpendicular to the borehole (e.g. *SHmax* = *Shmin* in the case of a vertical borehole) the stress around the borehole in function of the angle θ is constant. This implies in terms of wellbore failure only two possibilities: either the stress state at the borehole wall is below the failure criteria and no failure occur or the stress state at the borehole wall is higher than the failure criteria and failure occur for all θ, i.e. $2\theta_b = 180^\circ$ (complete circumferential failure of the wellbore wall). This is why for an isotropic stress state in the plane perpendicular to the borehole, the breakout width contours converge to one single point. More precisely, this point denotes the smallest transversely-isotropic far-field stress magnitude that will produce failure at all points around the borehole, given the prevailing cooling, and pore- and wellbore pressure conditions prevailing. It is computed by solving Eqs. (6), (10) and (11), which leads to:

$$Shmin = SHmax = \frac{C_o + Pw + \beta Pp - S_\theta^{\Delta T}}{2} \tag{22}$$

Using the above approach, bounds on *Shmin* and *SHmax* were computed using the same strength and effective stress parameters as in the example of Fig. 13, and the results displayed in Fig. 14. The effective stress law for tensile failure is chosen in order to provide conservative bounds on the stress estimate, i.e. β_t= 1.0 where DITFs occurs and β_t= 0.0 where they are absent. Cooling profiles for compressive and tensile failure to compute the thermal stresses in this analysis (Fig. 10) are taken as the central line (average) of the possible cooling values evaluated earlier (grey areas on Fig. 10). The results are broadly consistent with the *SHmax* profiles derived from the breakout width analyses in Fig. 11, but have the advantage of imposing independent constraints on the *Shmin* magnitude. The *Shmin* estimates at locations where either breakouts and DITFs, DITFs only, or no wellbore failure occurs are consistent with the linear trend in *Shmin* that was constrained by the limiting pressure at the casing shoe during stimulation (black square on Fig. 14) and forced through the origin (i.e. the profile denoted '*Shmin*-hydraulic' in Fig. 14). However, the *Shmin* estimates at locations where only breakouts are observed are for the most part significantly greater than the linear profile, the trend of the *Shmin* estimates displaying a flatter gradient whose lower limit approaches the linear profile towards the bottom of the well. This lower limit is not in disagreement with the limiting pressure measurement at the casing shoe. The uncertainty on the constraints in each stress estimate represent the bounds on *Shmin-SHmax* solution space imposed by the observed failure. The discontinuous nature of the modes of wellbore failure implies stress heterogeneity. The best stress estimates come from small areas of overlap in the solution spaces from different failure combinations. Trend lines have been added to Fig. 14 by visual adjustment of linear trends attempting to be in agreement with most constraints. They suggest a gradient of 7 MPa/km for *Shmin* and a 5 MPa/km for *SHmax*. This gradient is surprisingly low for both *Shmin* and *SHmax* confirming the results obtained above (Fig. 11) for the analysis of breakout width only. It is, however, important to note that the stress magnitude constraints obtained from this method are largely controlled by the lower frictional limit on crustal strength and the breakout width singularity point, which is dependent upon borehole wall strength, pore and wellbore pressures, and cooling, as discussed above.

5. Discussions

A common feature of all the computed *SHmax* profiles is the very low or even slightly negative gradient with depth. All of the conducted analyses suggest that the *SHmax* gradient is 5 MPa/km at most. The low gradient is a consequence of the observation that breakout width decreases with depth. Changing the slope of the *Shmin* profile within reasonable bounds from that of Eq. (2) does not change this result as

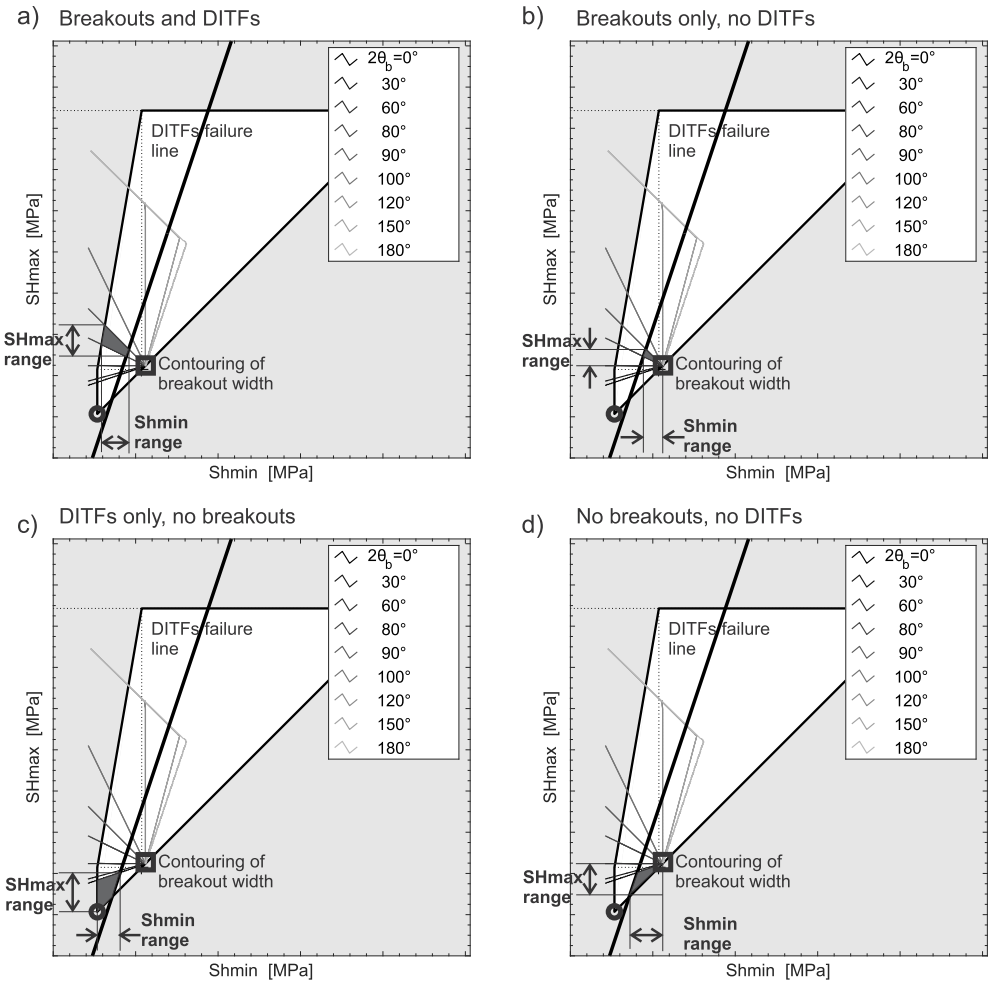

Fig. 13. Hypothetical example illustrating how each of the four possible combinations of failure/no-failure set constraints on both *Shmin* and *SHmax* magnitudes: a) simultaneous occurrence of borehole breakouts (with width θ_b = 80–90°) and DITFs; b) Occurrence of borehole breakouts (with width θ_b = 80–90°) but no DITFs, c) occurrence of DITFs but no breakouts ($\theta_b \leq 0°$); and d) Absence of breakouts ($\theta_b \leq 0°$) and DITFs. Such diagram must be computed at each depth and the position of the stress polygon and absolute values of *Shmin* and *SHmax* (voluntary not given here) will vary depending on the vertical stress and pore pressure estimate at the given depth.

illustrated by Valley and Evans.[67] Determining the *Shmin* profile independently from hydraulic tests by considering conjointly the breakout width and the presence or absence of DITFs (Fig. 14) suggests that *Shmin* also has a low gradient of about 7 MPa/km, although this result is largely dependent on the assumed cooling profile for the formation of DITFs. Adoption of a profile where the cooling is much lower in the upper section of the well can increase the *Shmin* gradient by to up to 12 MPa/km, but not more.

Purely gravitational loading of an isotropic, homogeneous elastic half-space with zero horizontal strain boundary conditions would induce a horizontal to vertical stress ratio given by $\frac{\nu}{(1-\nu)}$. Although this model is generally considered too simplistic to represent natural conditions in geologic situations, it is used here to evaluate its consequences in terms of stress gradient. Considering the vertical stress gradient given in Eq. (1) and a Poisson's ratio in the range ν = 0.3 to 0.35 would imply a horizontal stress gradient of 11–13 MPa/km. More complex stress models like the elasto-static thermal stress model of Sheorey[68] predict almost constant horizontal to vertical stress ratio in the range of 0.45–1.1 (depending on the assumed crust stiffness) for depth larger than 3 km. A uniform tectonic straining of a homogeneous linearly-elastic material will modify the stress magnitude but not the stress gradient. Stiffness contrast will affect the stress gradient. In the case of the basement below Basel, it is conceivable that the upper 400 m of the basement is more compliant due to more intense fracturing.[69] However, for a uniform straining, a stiffness gradient going from relatively compliant rocks close to the cover-basement interface toward stiffer rocks below would induce a steepening of the horizontal stress gradient and would not be consistent with the low gradient observed. The observed reduction of horizontal stress gradient would require a tectonic strain gradient, with more intense straining at the cover-basement interface and a reduction of the tectonic straining with depth. Such a strain gradient would require a drag of the top basement occurring below the décollement level at the base of the Mesozoic strata in the Triassic evaporites. It has been shown that a perturbation to the stress field occurs at the basement-cover interface,[17] although the origin of the perturbation is not well understood and is beyond the scope of this paper. Although the BS-1 borehole is located close to large scale tectonic boundaries that are the frontal thrust of the Jura fold-and-thrust belt and the Upper Rhine Graben east border fault, it is not obvious to anticipate what combined effects the proximity to these structures might have on the local stress field. Large scale stress models developed for the area do not provide additional insights since they focus on stress variations within the sedimentary cover[70] or the effect at the asthenosphere-lithosphere boundary.[71]

The *SHmax* profiles derived from breakout width alone using each of the four failure criteria are shown in Fig. 11. Although the *SHmax* gradients are similar, the absolute magnitudes differ significantly.

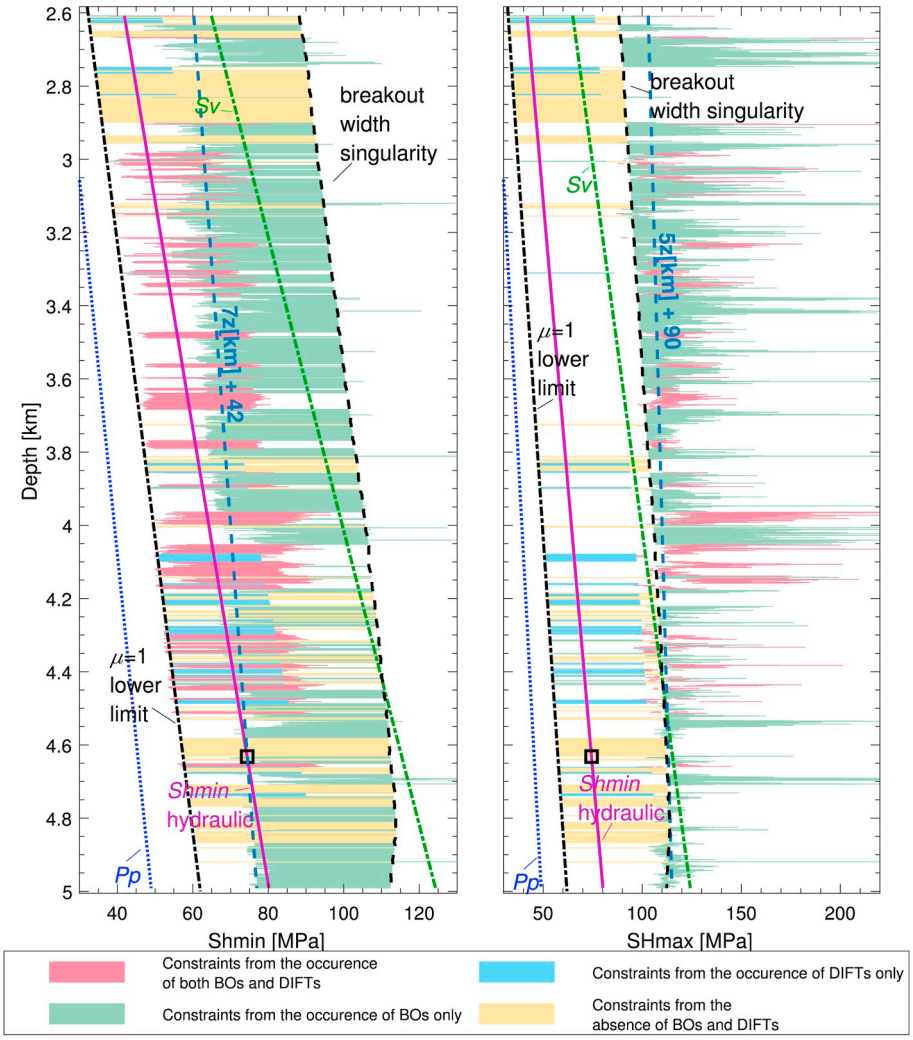

Fig. 14. Simultaneous constraints on *Shmin* and *SHmax* magnitude profiles given by the presence or absence of borehole breakouts and DITFs. This computation assumes a compressive strength given by the low confinement Mohr-Coulomb/Rankine with $C_o^R = C_o = 117.7$ MPa, a tensile strength $T = 4$ MPa for the formation of DITFs and mean cases from the ranges relevant for compressive and tensile failure presented on Fig. 10 for the thermally induced stresses. The black square denotes the maximum pressure reached during the stimulation injection at casing shoe and is considered to be a reliable estimate of the Shmin magnitude, the profile of which is denoted as 'Shmin-hydraulic'.

Specifically, the Mogi-Coulomb (Fig. 11c) and Hoek-Brown-3D (Fig. 11d) criteria that consider the strengthening effect of the intermediate principal stress lead to *SHmax* estimates that are 60–80 MPa higher than for the low strength Mohr-Coulomb criterion (Fig. 11a) and 25–50 MPa higher than for the high strength Mohr-Coulomb case (Fig. 11b). The *SHmax* magnitude estimates for (Fig. 11c) and (Fig. 11d) at depths above 4200 m exceed the upper limit set by assigning a Coulomb friction strength for the crust with a friction coefficient of 1.0, and as such are considered unacceptable. In contrast, profile (Fig. 11b) derived from the Mohr-Coulomb/Rankine criterion with the higher C_0 exceeds this limit only at the uppermost few tens of meters, whereas profile (Fig. 11a) for the Coulomb/Rankine criterion with the lower C_0 does not violate this upper limit.

The stress regimes implied by the *SHmax* profiles in Fig. 11 for the Mogi-Coulomb (Fig. 11c) and Hoek-Brown-3D (Fig. 11d) criteria are essentially strike-slip for the entire depth range (a possible exception applies for sections without breakouts where only an upper bound for *SHmax* can be derived). The *SHmax* profile for the Mohr-Coulomb criterion with higher C_0 (Fig. 11b) trends from a strike-slip regime above 4200 m to mixed strike-slip/normal faulting below 4200 m. The *SHmax* profile for the Mohr-Coulomb criterion with lower C_0 (Fig. 11a) crosses over from a predominantly strike-slip regime above 4100 m to a predominantly normal faulting regime below 4500 m. These results can be compared with the depth trends of faulting style derived from focal mechanisms analyses. A catalog of 28 focal mechanisms determined by Deichmann and Ernst[21] using the polarity of the first P-wave arrivals for the stronger events recorded during the stimulation of the BS-1 borehole was extended to 118 focal mechanisms in Terakawa et al.[22] This data set is dominated by strike-slip faulting style with some normal component but little or no thrust component. No clear depth trend is recognizable on this data set, although depth localization uncertainty was less than 50 m neat the casing shoe thanks to the presence of a 3-component clamp sensor at the wellbore casing shoe. A larger focal mechanism set including 639 events was derived by Kraft and

Deichmann[23] using P- and S-wave amplitudes in addition to p-wave first motion polarities to constrain the focal mechanism. This dataset contains a mix of normal and strike-slip focal mechanism as well as a few thrust events. No depth trend is present concerning the balance between normal and strike-slip mechanisms, suggesting that *SHmax* magnitude is not greatly different from *Sv*. A few predominantly thrust component mechanisms were resolved, but all are confined to the upper part of the granite above the liner shoe at 4632 m depth, suggesting that *Shmin* is closer to *Sv* in the upper part of the profile than in the lower part. This might be taken as consistent with a relatively small gradient for *Shmin*, similar to the small gradient derived for *SHmax*.

The *SHmax* profile that is most consistent with independent constraints is the one derived using a Mohr-Coulomb/Rankine failure criterion with the strength at the borehole wall given by the lower of the two estimates of uniaxial compressive strength C_0 derived from the strength data of Table 1. This is the only profile that does not violate bounds on admissible *SHmax* values imposed by widely-accepted frictional limits to the strength of the crust, and it is also fully consistent with the depth trend of faulting style derived from focal mechanisms of micro-earthquakes induced in the reservoir during stimulation. This *SHmax* profile, like all others, has a very small depth gradient. Based on the results shown Figs. 11 and 14, we propose linear depth trends for *Shmin* and *SHmax* in the depth range 2500–5000 m given by:

$$Shmin\,[MPa] = 7z\,[km] + 42 \tag{23}$$

$$SHmax\,[MPa] = 5z\,[km] + 90 \tag{24}$$

It should be emphasized that the validity of the absolute magnitude derived from these profiles depends strongly on the strength assumptions adopted, while the stress gradients are independent of the strength assumptions, as discussed above. To improve confidence in the absolute stress magnitude estimates from breakout geometry would require a better understanding of which failure model properly captures breakout formation in low porosity crystalline rocks, and how to parametrize such a model. The former would benefit from well controlled in-situ experiments in full scale boreholes. Laboratory experiments conducted on small samples[72] have given valuable insights as to the failure processes, but upscaling the results to full scale field cases remains uncertain. The study presented here also highlights the importance of securing high-quality rock strength data in future deep borehole projects in order to parametrize the strength criteria. This will remain challenging because cores, if collected from depth relevant for breakout formation, are likely to contain micro-damage that will affect the strength parametrization. An alternate approach is to estimate strength from geophysical logging as proposed for example by Chang et al.,[31,73] but the universal validity of such relationship and their robustness in crystalline hard rock has not yet been demonstrated.

An obvious feature of all horizontal stress profiles is the persistent small-scale fluctuations in stress magnitude that arise from fluctuations in breakout width and the variation of style of wellbore failure (i.e. absence or presence of breakouts and/or DITFs). Taken on face value, the breakout-width fluctuations would imply *SHmax* variations of several tens of MPa depending upon the failure criterion used. However, in reality, the variation in breakout width is likely to reflect both stress and strength variations along the borehole. Fabbri[74] and Sikaneta and Evans[75] found changes in breakout width in the BS-1 borehole often correlated with locations where fracture or fracture zones cut the well, but note that the variations could reflect reduced strength due to alteration and damage, or perturbation in stress magnitudes associated with fractures. In the current state of knowledge, differentiation of stress vs. strength effects on breakout width is not possible without independent knowledge of one or the other. Thus, variations in breakout width or variation of the style of wellbore failure should not be interpreted as solely reflecting stress heterogeneity.

6. Conclusions

The wellbore failure dataset from the 5 km deep sub-vertical borehole BS-1 is exceptional because near-continuous breakouts occur over 81% of the lowermost 2.4 km of hole in monzogranite, together with more sporadic drilling-induced tension fractures (DITFs). We have analysed the dataset using two approaches to obtain estimates of stress magnitude. Both approaches are reliant on the simplifying assumption that breakout width can be related to the stresses resolved at the surface of a cylindrical vertical wellbore in a uniform, isotropic poro-elastic medium. The wellbore wall stresses arise from the far-field principal stresses (i.e. the vertical, *Sv*, and maximum and minimum horizontal stresses, *SHmax* and *Shmin* respectively), the wellbore fluid pressure, *Pw*, and cooling stresses arising from the drilling operation. Breakout width is determined in the model by identifying the sectors of the borehole wall where the resolved effective stresses reach the compressive failure criterion. Similarly, the presence or absence of DITFs is tested by assessing whether the resolved effective stresses at any point on the wellbore wall meet the criterion for tensile failure. No consideration is given to the possible effect of the evolving geometry of a breakout during its formation in modifying the stresses at the wellbore that govern breakout width.

In the first approach, hydraulic observations were used to define a profile of minimum principal horizontal stress, *Shmin*, along the borehole and the observed breakout width used to estimate a profile of maximum principal horizontal stress, *SHmax*. Four different failure criteria for the borehole wall were considered: the Rankine that considers only the maximum stress at the borehole wall, the Mohr-Coulomb that considers that maximum and minimum stress, and the Mogi-Coulomb and Hoek-Brown criteria that take in consideration the strengthening effect of the intermediate principal stress. All were parametrized using data from a multi-stage confined compression tests performed on a single core plug taken from 4902 m depth. The resulting profiles show significant small-scale variations in *SHmax* magnitude which reflect variations in breakout width. These tend to correlate with fractures and fracture zones intersected by the borehole, and may in part at least reflect changes in rock wall strength at the structures which are not included in the modeling. Thus, the small-scale variations in the SHmax profiles cannot be taken as a direct measure of stress variability. A surprising observation is that at large scales, where the rock strength can be taken as reasonably constant, breakout width tends to decrease systematically with depth. As a consequence, the large-scale trends of the *SHmax* profiles obtained from the stress inversions using each of the four failure criteria were found to have a very low gradient. This result is independent of the *Shmin* profile used in the analysis. The large-scale trends of the SHmax profiles differ in terms of the stress magnitude. Inversions that use failure criteria that take in consideration the strengthening effect of the intermediate principal stress yield relatively high *SHmax* magnitudes that violate limits imposed by the strength of the crust characterized by a Coulomb friction criterion with a friction coefficient of $\mu = 1.0$. In contrast, the profiles obtained using the Mohr-Coulomb/Rankine criteria which ignore the intermediate principal stress do not and are thus preferred.

In the second approach, the breakout width profile, which includes sections with zero width (i.e. no breakout), was combined with the DITF profile (i.e. existence of otherwise at each depth), and pairs of values of *Shmin* and *SHmax* magnitude that were consistent with the observed pattern of failure (i.e. presence of both DITFs and breakouts with their width, breakouts only with their width, DITFs only, or no failure) were determined at each depth. The computations were performed for the Mohr-Coulomb compressive failure criterion that yielded

the best results in the first approach, and a coefficient in the effective stress law for tensile failure of 1.0 when DITFs are present and 0.0 when DITFs are absent which leads to the most conservative estimate. The results are consistent with the first approach inasmuch as they indicate a low gradient for the *SHmax* profile. They also suggest a low gradient for *Shmin*, however this latter result is largely influence by the estimate of cooling for DITFs formation, a parameter that is not well constrained in the upper section of the borehole.

The depth trend of *SHmax* indicated that strike-slip faulting predominates above 4200 m and strike-slip/normal faulting below. This is reasonably consistent with focal mechanisms recorded during the reservoir stimulation which show a mix of strike-slip and normal faulting throughout the depth range considered. There is no obvious geological or tectonic explanation of the low gradient of the *SHmax* profile.

Some circumspection of the results is warranted in our opinion as the breakout formation process in crystalline rocks is not sufficiently well understood, and basic assumptions commonly made when inverting stress from breakout width may not be valid: for example, the assumption that the initial and final width of the breakouts are identical, and that the tangent stress around the wellbore is not significantly affected by the evolving geometry of the borehole cross-section during breakout development. In addition, the absolute magnitude derived from such analyses depends strongly on the strength model used and its parameterization. In that regard, the limited data available for the BS-1 borehole highlight the importance of obtaining a more extensive strength characterization in future deep borehole projects. Nonetheless, the conclusion of a low gradient of *SHmax* appears to be robust as it is forced by the observation that breakout width decreases with depth.

Acknowledgements

We thank Geo-Energy Suisse for permission to publish these data and Florentin Ladner for fruitful discussions. Chandong Chang and two others anonymous reviewers provided valuable comment to improve the final version of the paper. This work was funded by the GEOTHERM-2 research program supported by the Competence Center for Environment and Sustainability (CCES) and the Competence Center Energy and Mobility (CCEM) of ETH Domain, and the Swiss Federal Office of Energy. Benoît Valley acknowledges support from the Swiss Competence Center in Energy Research – Supply of Electricity (SCCER-SoE).

Appendix. Estimation of bottom hole temperature from EMS survey

Electronic Multishot Surveys (EMS) are primarily intended to measure the profile of hole trajectory, and are run prior to pulling the drill string out of the hole for a bit change or other operation on the bottom hole assembly (BHA). Three EMS records were acquired when the borehole depth was 4429 m, 4687 m and 4988 m, and the resulting temperature profiles are shown in Fig. 10a by dotted lines with triangles, circles and diamonds respectively. Note that these are not conventional temperature logs. The EMS measurement principle is as follows. First, the probe clock and sample period is set and the probe inserted into the top of the drilling string. Mud circulation helps the probe descend, and it lands in the bottom hole assembly, close to the hole bottom, at which point the mud circulation is stopped. The drill string is then progressively built out of the hole, thereby bringing the probe slowly to the surface. The probe position at any time can be determined by comparing clock time with the time record of BHA position. The probe is not necessarily always in thermal equilibrium with the drilling mud. However, for the measurements of greatest importance here, those of bottom-hole temperature, a check of equilibration can be made because the probe sits stationary within the BHA for a sufficiently long time before pulling-out begins to capture the temperature rise to equilibrium (horizontal dotted lines on Fig. 10a). This can be seen in the equilibration curves for the bottom-hole measurement from the three surveys presented in Fig. A-1 which show an equilibration time of 45–75 min. The equilibrated temperatures at the hole bottom for these surveys at 4429 m, 4687 m and 4988 m are 84 °C, 83.5 °C and 89 °C respectively.

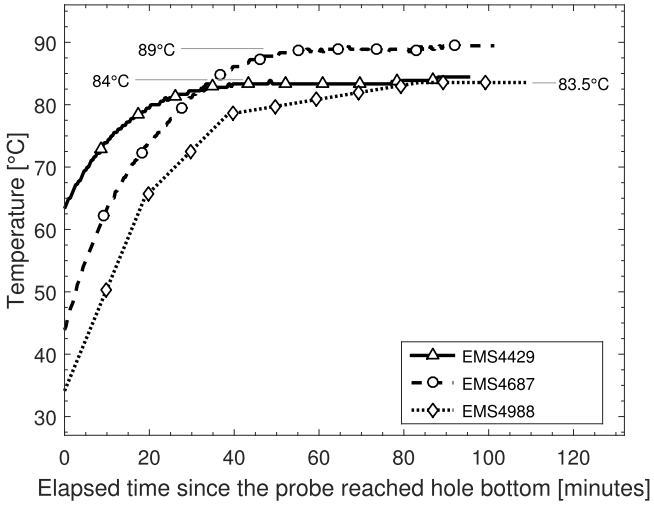

Fig. A-1. Thermal equilibration of the EMS probe when sitting in the bottom hole assembly. About 45–75 min are required for the probe to equilibrate with the ambient temperature.

Sensitivity of the stress estimate on the strength values

The estimation of borehole wall strength is a central issue in stress estimation from wellbore failure. Experimental work suggest that test performed on dry jacketed samples such as we used in our analyses may provide an overestimate of the borehole strength by up to about 50%.[7,46] In order, to evaluate the implications that such a strength overestimation would have on our analyses, we performed a sensitivity study.

In a first step, we determined the parameters of the strength criteria by reducing the peak strength measurement to 85%, 70% and 55% of the reported peak strength. An example of such processing is given for the Mohr-Coulomb criteria in Fig. A-2. A similar approach was performed for the other criteria and the parameter values are summarized in Table A-1.

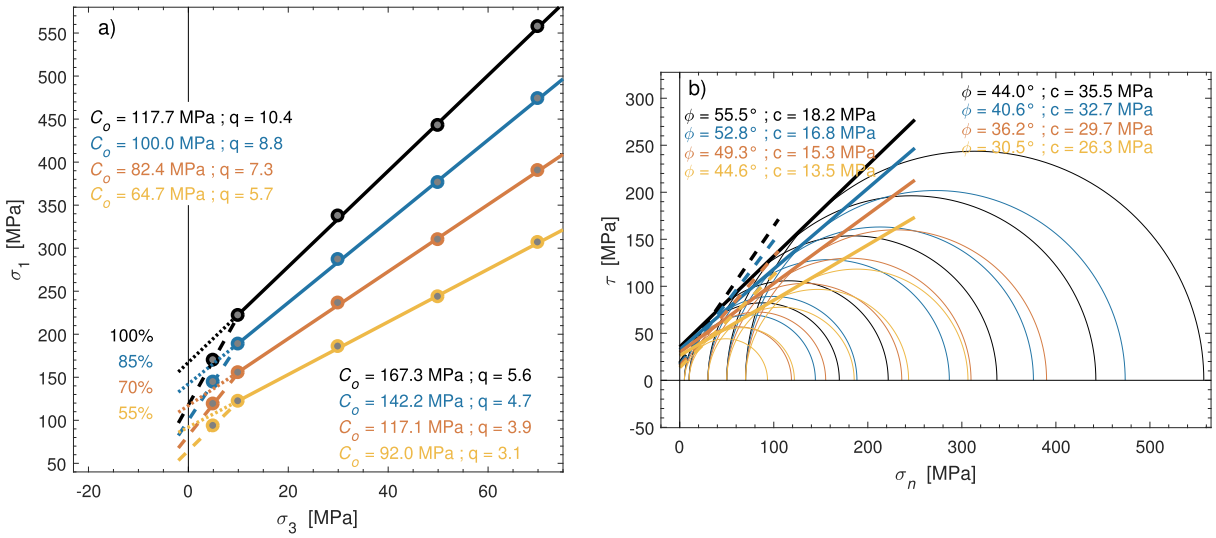

Fig. A-2. Estimation of the reduced strength parameters obtained by fitting the Mohr-Coulomb failure criteria to peak strength reduced to 85%, 70% and 55% of the reported strength. Compare with Fig. 5.

Using the reduced strength parameters listed in Table A-1, stress estimates derived from breakout width were computed in the same manner as for Fig. 11. This sensitivity analyses is presented in Fig. A-3. Evidently a reduction in strength results in reduced stress estimates. However, the slopes of the linear trends are almost unaffected by the strength reduction.

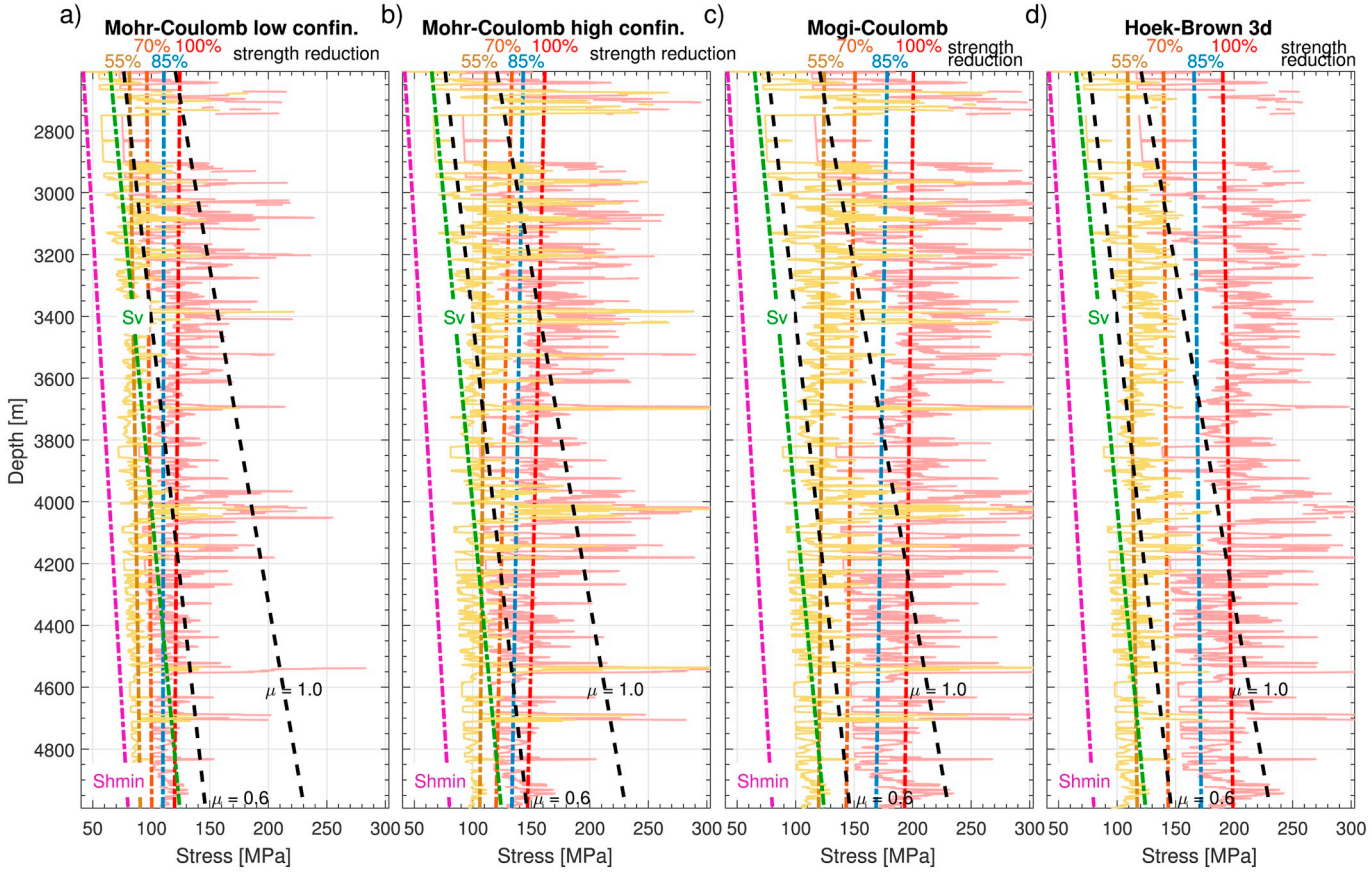

Fig. A-3. Computation of stress from borehole breakout width with a sensitivity study on the wellbore strength. The stress profiles have been computed in the same manner as for Fig. 11. Here for readability, not all curves are presented. We show principally the linear trend for SHmax for various strength scenarios. For the highest (100%) and the lowest (55%) strength scenarios, we show also the filtered result using a 7-points (2.8 m) moving average in order to illustrate the variability of the estimates. For the other curves, refer to Fig. 11.

Table A-1
Strength parameters estimated for reduced peak strength values.

	Mohr-Coulomb low confin.		Mohr-Coulomb high confin.		Mogi-Coulomb		Hoek-Brown	
	Co [MPa]	q [−]	Co [MPa]	q [−]	a	b	Co [MPa]	mi
100%	117.7	10.4	167.3	5.6	21.26	0.67	109.0	27.7
85%	100.0	8.8	142.2	4.7	20.73	0.63	95.4	21.6
70%	82.4	7.3	117.1	3.9	20.01	0.57	81.7	15.8
55%	64.7	5.7	92.0	3.1	19.00	0.49	67.6	10.3

References

1. Zoback MD, Barton CA, Brudy M, et al. Determination of stress orientation and magnitude in deep wells. *Int J Rock Mech Min Sci.* 2003;40(7):1049–1076. https://doi.org/10.1016/j.ijrmms.2003.07.001.
2. Schmitt DR, Currie CA, Zhang L. Crustal stress determination from boreholes and rock cores: fundamental principles. *Tectonophysics.* 2012;580(Supplement C):1–26. https://doi.org/10.1016/j.tecto.2012.08.029.
3. Ask D. New developments in the Integrated Stress Determination Method and their application to rock stress data at the Äspö HRL, Sweden. *Int J Rock Mech Min Sci.* 2006;43(1):107–126. https://doi.org/10.1016/j.ijrmms.2005.04.011.
4. Mastin L, Heinemann B, Krammer A, Fuchs K, Zoback M. Stress orientation in the KTB pilot hole determined from wellbore breakouts. *Sci Drill.* 1991;2(1991):1–12.
5. Brudy M, Zoback MD. Compressive and Tensile failure of boreholes arbitrarily-inclined to principal stress axes: application to the KTB boreholes, Germany. *Int J Rock Mech Min Sci Geomech Abstr.* 1993;30(7):1035–1038.
6. Borm G, Engeser B, Hoffers B, Kutter HK, Lempp C. Borehole instabilities in the KTB main borehole. *J Geophys Res Solid Earth.* 1997;102(B8):18507–18517. https://doi.org/10.1029/96JB03669.
7. Vernik L, Zoback MD, Brudy M. *Methodology and Application of the Wellbore Breakout Analysis in Estimating the Maximum Horizontal Stress Magnitude in the KTB Pilot Hole.* 1992; 1992https://publikationen.bibliothek.kit.edu/67492, Accessed date: 13 November 2018.
8. Vernik L, Zoback MD. Estimation of maximum horizontal principal stress magnitude from stress-induced well bore breakouts in the Cajon pass scientific research borehole. *J Geophys Res.* 1992;97(B4):5109–5119.
9. Shamir G, Zoback MD. Stress orientation profile to 3.5 km depth near the san andreas fault at Cajon pass, California. *J Geophys Res Solid Earth.* 1992;97(B4):5059–5080. https://doi.org/10.1029/91JB02959.
10. Bérard T, Cornet FH. Evidence of thermally induced borehole elongation: a case study at Soultz, France. *Int J Rock Mech Min Sci.* 2003;40(7):1121–1140. https://doi.org/10.1016/S1365-1609(03)00118-7.
11. Cornet F, Bérard T. *A Case Example of Integrated Stress Profile Evaluation.* Balkema; 2003.
12. Valley B, Evans KF. Stress state at Soultz to 5km depth from wellbore failure and hydraulic observations. *EHDRA Scientific Conference, 15–16 June 2006. Soultz-Sous-Forêts, France.* 2006; 2006.
13. Valley B, Evans KF. Stress state at Soultz-sous-Forêts to 5 km depth from wellbore failure and hydraulic observations. *32nd Workshop on Geothermal Reservoir Engineering. Stanford.* 2007; 2007.
14. Fernández-Ibáñez F, Castillo D, Wyborn D, Hindle D. Benefits of HT-hostile senvironements on wellbore stability: a case study from geothermal fields in central Australia. *Proceedings of the 33rd Annual Convention and Exhibition of the Indonesian Petroleum Association.* 2009; 2009.
15. Häring MO, Schanz U, Ladner F, Dyer BC. Characterisation of the Basel 1 enhanced geothermal system. *Geothermics.* 2008;37(5):469–495. https://doi.org/10.1016/j.geothermics.2008.06.002.
16. Evans KF, Roth P. *The State of Stress in Northern Switzerland Inferred from Earthquake Seismological Data and In-Situ Stress Measurements.* Sewardstrasse 7, CH-8050, Switzerland: Proseis AG; 1998.
17. Valley B, Evans K. Stress orientation to 5 km depth in the basement below Basel (Switzerland) from borehole failure analysis. *Swiss J Geosci.* 2009;102(3):467–480. https://doi.org/10.1007/s00015-009-1335-z.
18. Kastrup U, Zoback ML, Deichmann N, Giardini D, Evans KF, Michael AJ. Stress field variations in the Swiss Alps and the northern Alpine foreland derived from inversion of fault plane solutions. *J Geophys Res.* 2004;109(B01402).
19. Plenefisch T, Bonjer K-P. The stress field in the Rhine Graben area inferred from earthquake focal mechanisms and estimation of frictional parameters. *Tectonophysics.* 1997;275(1–3):71–97. https://doi.org/10.1016/S0040-1951(97)00016-4.
20. Deichmann N, Giardini D. Earthquakes induced by the stimulation of an enhanced geothermal system below Basel (Switzerland). *Seismol Res Lett.* 2009;80(5):784–798. https://doi.org/10.1785/gssrl.80.5.784.
21. Deichmann N, Ernst J. Earthquake focal mechanisms of the induced seismicity in 2006 and 2007 below Basel (Switzerland). *Swiss J Geosci.* 2009;102(3):457–466. https://doi.org/10.1007/s00015-009-1336-y.
22. Terakawa T, Miller S, Deichmann N. High fluid pressure and triggered earthquakes in the enhanced geothermal system in Basel, Switzerland. *J Geophys Res.* 2012;117(B7):B07305https://doi.org/10.1029/2011jb008980.
23. Kraft T, Deichmann N. High-precision relocation and focal mechanism of the injection-induced seismicity at the Basel EGS. *Geothermics.* June 2014. https://doi.org/10.1016/j.geothermics.2014.05.014.
24. Braun R. *Analyse Gebirgsmechanischer Versagenszustände Beim Geothermieprojekt Basel Report to Geopower Basel AG for Swiss Deep Heat Mining Project Basel 2007; 2007 30+.*
25. Zang A, Stephansson O. *Measuring Crustal Stress: Core-Based Methods. Stress Field Earths Crust.* 2010; 2010:165–191.
26. Schärli U, Kohl T. *Archivierung Und Kompilation Geothermischer Daten Der Schweiz Und Angrezender Gebiete.* Schweizerische Geophysikalische Kommission; 2002.
27. Lin W, Yamamoto K, Ito H, Masago H, Kawamura Y. Estimation of minimum principal stress from an extended leak-off test onboard the chikyu drilling vessel and suggestions for future test procedures. *Sci Drill.* 2008;6:43–47. https://doi.org/10.2204/iodp.sd.6.06.2008.
28. Schmitt DR, Haimson B. Hydraulic fracturing stress measurements in deep holes. *Rock Mechanics and Engineering.* vol. 1. 2017; 2017https://doi.org/10.1201/9781315364261-7.
29. Barton C, Zoback M, Burns K. In-situ stress orientation and magnitude at the Fenton geothermal site, New Mexico, determined from wellbore breakouts. *Geophys Res Lett.* 1988;15(5):467–470.
30. Martin CD, Stimpson B. The effect of sample disturbance on laboratory properties of Lac du Bonnet granite. *Can Geotech J.* 1994;31(5):692–702. https://doi.org/10.1139/t94-081.
31. Chang C, Zoback MD, Khaksar A. Empirical relations between rock strength and physical properties in sedimentary rocks. *J Pet Sci Eng.* 2006;51(3-4):223–237. https://doi.org/10.1016/j.petrol.2006.01.003.
32. Zoback MD, Apel R, Baumgärtner J, et al. Upper-crustal strength inferred from stress measurements to 6 km depth in the KTB borehole. *Nature.* 1993;365(6447):633–635. https://doi.org/10.1038/365633a0.
33. Lofts JC, Bourke LT. The recognition of artefacts from acoustic and resistivity borehole imaging devices. *Geol Soc Lond Spec Publ.* 1999;159(1):59–76. https://doi.org/10.1144/gsl.sp.1999.159.01.03.
34. Hiramatsu Y, Oka Y. Determination of the stress in rock unaffected by boreholes or drifts, from measured strains or deformations. *Int J Rock Mech Min Sci.* 1968;5:337–353.
35. Kirsch G. Die theorie der elastizitat und die bedurfnisse der festigkeitslehre. *Z Ver Dtsch Ingenieure.* 1898;42:797–807.
36. Stephens G, Voight B. Hydraulic fracturing theory for conditions of thermal stress. *Int J Rock Mech Min Sci Geomech Abstr.* 1982;19(6):279–284. https://doi.org/10.1016/0148-9062(82)91364-X.
37. Evans KF, Scholz CH, Engelder T. An analysis of horizontal fracture initiation during hydrofrac stress measurements in granite at North Conway, New Hampshire. *Geophys J Int.* 1988;93(2):251–264. https://doi.org/10.1111/j.1365-246X.1988.tb02000.x.
38. Nelson EJ, Meyer JJ, Hillis RR, Mildren SD. Transverse drilling-induced tensile fractures in the West Tuna area, Gippsland Basin, Australia: implications for the in situ stress regime. *Int J Rock Mech Min Sci.* 2005;42(3):361–371. https://doi.org/10.1016/j.ijrmms.2004.12.001.
39. Colmenares LB, Zoback MD. A statistical evaluation of intact rock failure criteria constrained by polyaxial test data for five different rocks. *Int J Rock Mech Min Sci.* 2002;39(6):695–729.
40. Zhang C, Zhou H, Feng X, Huang S. A new interpretation for the polyaxial strength effect of rock. *Int J Rock Mech Min Sci.* January 2010. https://doi.org/10.1016/j.ijrmms.2010.01.003.
41. Eissa EA, Kazi A. Relation between static and dynamic Young's moduli of rocks. *Int J Rock Mech Min Sci Geomech Abstr.* 1988;25(6):479–482. https://doi.org/10.1016/0148-9062(88)90987-4.
42. Cooper HW, Simmons G. The effect of cracks on the thermal expansion of rocks. *Earth Planet Sci Lett.* 1977;36(3):404–412. https://doi.org/10.1016/0012-821X(77)90065-6.
43. Huotari T, Kukkonen I. *Thermal Expansion Properties of Rocks: Literature Survey and Estimation of Thermal Expansion Coefficient for Olkiluoto Mica Gneiss.* Posiva; 2004:62.
44. Bieniawski ZT, Bernede MJ. Suggested methods for determining the uniaxial compressive strength and deformability of rock materials. *Int J Rock Mech Min Sci Geomech Abstr.* 1979;16(2):138–140. https://doi.org/10.1016/0148-9062(79)91451-7.
45. Darlington W, Ranjith P, Choi S. The effect of specimen size on strength and other properties in laboratory testing of rock and rock-like cementitious brittle materials. *Rock Mech Rock Eng.* 2011;44(5):513–529. https://doi.org/10.1007/s00603-011-0161-6.
46. Chang C, Haimson B. Effect of fluid pressure on rock compressive failure in a nearly impermeable crystalline rock: implication on mechanism of borehole breakouts. *Eng*

Geol. 2007;89(3):230–242. https://doi.org/10.1016/j.enggeo.2006.10.006.
47. Brace WF, Martin RJ. A test of the law of effective stress for crystalline rock of low porosity. *Int J Rock Mech Min Sci.* 1968;5(5):415–426.
48. Schmitt DR, Zoback MD. Poroelastic effects in the determination of the maximum horizontal principal stress in hydraulic fracturing tests–A proposed breakdown equation employing a modified effective stress relation for tensile failure. *Int J Rock Mech Min Sci Geomech Abstr.* 1989;26(6):499–506.
49. Schmitt DR, Zoback MD. Diminished pore pressure in low-porosity crystalline rock under tensional failure; apparent strengthening by dilatancy. *J Geophys Res.* 1992;97(1):273–288.
50. Schmitt DR, Zoback MD. Infiltration effects in the tensile rupture of thin walled cylinders of glass and granite: implications for the hydraulic fracturing breakdown equation. *Int J Rock Mech Min Sci Geomech Abstr.* 1993;30(3):289–303.
51. Bruno MS, Nakagawa FM. Pore pressure influence on tensile fracture propagation in sedimentary rock. *Int J Rock Mech Min Sci Geomech Abstr.* 1991;28(4):261–273. https://doi.org/10.1016/0148-9062(91)90593-B.
52. Detournay E, Boone TJ. Discussion. *Int J Rock Mech Min Sci Geomech Abstr.* 1993;30(3):323–324. https://doi.org/10.1016/0148-9062(93)92734-8.
53. Walton G, Kalenchuk K, Hume C, Diederichs M. Borehole breakout analysis to determine the in-situ stress state in hard rock. *ARMA 2015, 49th US Rock Mechanics/Geomechanics Symposium.* 2015; 2015.
54. Hoek E, Brown ET. Practical estimates of rock mass strength. *Int J Rock Mech Min Sci.* 1997;34(8):1165–1186. https://doi.org/10.1016/S1365-1609(97)80069-X.
55. Al-Ajmi A, Zimmerman R. Relation between the Mogi and the Coulomb failure criteria. *Int J Rock Mech Min Sci.* 2005;42(3):431–439.
56. Mogi K. Fracture and flow of rocks under high triaxial compression. *J Geophys Res.* 1971;76(5):1255–1269. https://doi.org/10.1029/jb076i005p01255.
57. Hoek E, Bieniawski ZT. Brittle rock fracture propagation in Rock under compression. *Int J Fract Mech.* 1965;1(3):137–155.
58. Griffith AA. The phenomena of rupture and flow in solids. *Philos Trans R Soc London, Ser A.* 1920:163–198.
59. Zhang L, Zhu H. Three-dimensional Hoek-Brown strength criterion for rocks. *J Geotech Geoenviron Eng.* 2007;133(9):1128–1135. https://doi.org/10.1061/(asce)1090-0241(2007)133:9(1128).
60. Perras MA, Diederichs MS. A review of the tensile strength of rock: concepts and testing. *Geotech Geol Eng.* 2014;32(2):525–546. https://doi.org/10.1007/s10706-014-9732-0.
61. Valley B. *The Relation between Natural Fracturing and Stress Heterogeneities in Deep-Seated Crystalline Rocks at Soultz-Sous-Forêts.* 2007; 2007 (France). http://e-collection.ethbib.ethz.ch/view/eth:30407, Accessed date: 9 November 2014.
62. Hoek E, Martin CD. Fracture initiation and propagation in intact rock – a review. *J Rock Mech Geotech Eng.* 2014;6(4):287–300. https://doi.org/10.1016/j.jrmge.2014.06.001.
63. Ramsey JM, Chester FM. Hybrid fracture and the transition from extension fracture to shear fracture. *Nature.* 2004;428(6978):63–66. https://doi.org/10.1038/nature02333.
64. Bobich JK. *Experimental Analysis of the Extension to Shear Fracture Transition in Berea Sandstone.* 2005; 2005.
65. Valley B, Azzola J, Schmittbuhl J, Genter A. *Temporal Borehole Breakout Evolution and its Impact on Stress Estimation.* Seattle: ARMA; 2018.
66. Forsythe GE, Malcolm MA, Moler CB. *Computer Methods for Mathematical Computations.* Prentice-Hall; 1976.
67. Valley B, Evans K. Estimation of the stress magnitudes in Basel enhanced geothermal system. *Proceedings of the World Geothermal Congress 2015. Melbourne.* 2015; 2015.
68. Sheorey PR. A theory for in Situ stresses in isotropic and transverseley isotropic rock. *Int J Rock Mech Min Sci Geomech Abstr.* 1994;31(1):23–34.
69. Ziegler M, Valley B, Evans K. Characterisation of natural fractures and fracture zones of the Basel EGS reservoir inferred from geophysical logging of the basel-1 well. *Proceedings World Geothermal Congress 2015. Melbourne.* 2015; 2015.
70. Hergert T, Heidbach O, Reiter K, Giger SB, Marschall P. Stress field sensitivity analysis in a sedimentary sequence of the Alpine foreland, northern Switzerland. *Solid Earth.* 2015;6(2):533–552. https://doi.org/10.5194/se-6-533-2015.
71. Maury J, Cornet FH, Cara M. Influence of the lithosphere–asthenosphere boundary on the stress field northwest of the Alps. *Geophys J Int.* 2014;199(2):1006–1017. https://doi.org/10.1093/gji/ggu289.
72. Haimson B. Micromechanisms of borehole instability leading to breakouts in rocks. *Int J Rock Mech Min Sci.* 2007;44(2):157–173.
73. Chang C, McNeill LC, Moore JC, Lin W, Conin M, Yamada Y. In situ stress state in the Nankai accretionary wedge estimated from borehole wall failures. *Geochem Geophys Geosyst.* 2010;11(12) https://doi.org/10.1029/2010GC003261.
74. Fabbri S. *Correlation of Stress Variations and Natural Fractures in the Basel Geothermal Borehole.* 2011; 2011 (Switzerland).
75. Sikaneta S, Evans KF. Stress heterogeneity and natural fractures in the Basel EGS granite reservoir inferred from an acoustic televiewer log of the Basel-1 well. *Thirty-Seventh Workshop on Geothermal Reservoir Engineering.* Stanford University; 2012.